



Orbital Stability of Circumstellar Planets in Binary Systems

Billy Quarles¹, Gongjie Li¹, Veselin Kostov^{2,3}, and Nader Haghighipour⁴

¹Center for Relativistic Astrophysics, ²School of Physics, Georgia Institute of Technology, Atlanta, GA 30332, USA; billyquarles@gmail.com

²NASA Goddard Space Flight Center, Greenbelt, MD 20771, USA

³SETI Institute, 189 Bernardo Avenue, Suite 200, Mountain View, CA 94043, USA

⁴Institute for Astronomy, University of Hawaii-Manoa, Honolulu, HI 96822, USA

Received 2019 November 6; revised 2019 December 19; accepted 2019 December 23; published 2020 February 3

Abstract

Planets that orbit only one of the stars in stellar binary systems (i.e., circumstellar) are dynamically constrained to a limited range of orbital parameters, and understanding conditions on their stability is thus of great importance in exoplanet searches. We perform ~ 700 million N -body simulations to identify how stability regions depend on properties of the binary, as well as the starting planetary inclination and mean longitude relative to the binary orbit. Moreover, we provide grid interpolation maps and lookup tables for the community to use our results. Through Monte Carlo methods, we determine that planets with a semimajor axis $a_p \lesssim 8\%$ of the binary semimajor axis a_{bin} will likely be stable, given the known distribution of binary star parameters. This estimate varies in the Lidov–Kozai regime or for retrograde orbits to 4% or 10% of a_{bin} , respectively. Our method to quickly determine the circumstellar stability limit is important for interpreting observations of binaries using direct imaging with the *James Webb Space Telescope*, photometry with the *Transiting Exoplanet Survey Satellite*, or even astrometry with *Gaia*.

Unified Astronomy Thesaurus concepts: [Orbits \(1184\)](#); [Habitable planets \(695\)](#); [Exoplanet dynamics \(490\)](#); [Exoplanets \(498\)](#); [Binary stars \(154\)](#)

1. Introduction

Before the discovery and confirmation of the first exoplanet around a Sunlike star, 51 Peg b (Marcy & Butler 1995; Mayor & Queloz 1995), many theoretical investigations uncovered that planetary systems could stably orbit one star in a stellar binary despite the intense periodic forcing from the stellar companion (Szebehely 1980; Rabl & Dvorak 1988; Benest 1988a, 1988b, 1993). Around the same time, observers began using radial velocity techniques to probe for the existence of substellar companions; one of the first proposed candidates was γ Cep Ab (Campbell et al. 1988). The host star belonged to a binary system, γ Cep AB, which has a binary separation of only about 20 au. Walker et al. (1992) later attributed the radial velocity signal to stellar rotation due to the limits of the data, but more observations eventually confirmed the existence of γ Cep Ab (Hatzes et al. 2003). Before this confirmation, four exoplanets were discovered (55 Cnc Ab, τ Boo Ab, v And Ab, & 16 Cyg Bb) around a host star that is part of a more widely separated binary (Butler et al. 1997; Cochran et al. 1997).

The closest Sunlike stars to the solar system, α Cen AB, are part of a binary architecture similar that of to γ Cep AB, where numerical studies have explored the extent to which a stable planetary orbit can persist around each star over a wide range of initial conditions (Wiegert & Holman 1997; Andrade-Ines & Michtchenko 2014; Quarles & Lissauer 2016; Quarles et al. 2018a). However, the detection of planets in α Cen AB remains in dispute. Radial velocity observations of α Cen B have suggested that an Earth-mass planet orbited the star on a ~ 3.2 day orbit (Dumusque et al. 2012), but later studies revealed that the significance of the radial velocity signal changed dramatically when different methods were used to analyze the data (Hatzes 2013; Rajpaul et al. 2016). The formation of Earth-mass planets around either star in α Cen AB is also contentious, considering that the known planet

population in binary systems⁵ consists predominantly of Jupiter-mass planets, and decades of radial velocity measurements of α Cen AB favor Neptune–Saturn mass planets in the upper limit (Zhao et al. 2018). Early models of planet formation in α Cen AB showed that solar system–like formation conditions (embryos & planetesimals) could produce terrestrial planets (Quintana et al. 2002; Haghighipour & Raymond 2007). In contrast, Thébault et al. (2008) and Thébault et al. (2009) performed simulations of planetesimal growth in the α Cen system, where they determined that eccentricity pumping from the binary companion largely prevented growth and subsequent planet formations processes would be very difficult. Theoretical models by Zsom et al. (2011) also found that the presence of a binary companion would lower the total disk mass through truncation, in addition to the problems of planetesimal growth. However, it has been suggested that these issues could be avoided under a range of initial conditions including non-coplanar disks (Marzari et al. 2009; Xie et al. 2010; Rafikov 2013; Rafikov & Silsbee 2015). Future observations with the *James Webb Space Telescope* (JWST) could help resolve these disputes with a detection—or at least put stronger upper limits on the size of any potential worlds orbiting α Cen A (Beichman et al. 2020).

Ground-based observational studies have indicated that Sunlike stars are common among binary systems, where nearly half of Sunlike stars have a binary companion (Raghavan et al. 2010; Moe & Di Stefano 2017). The *Kepler Space Telescope* observed 2878 eclipsing binary systems, 1.3% of all targets, within the prime mission (Kirk et al. 2016), and discovered about a dozen *circumbinary* planets. Using the results from *Kepler*, Kraus et al. (2016) proposed that the apparent lack of *circumstellar* planets discovered with binary separations similar to γ Cep AB was due to the ruinous effects of the

⁵ <https://www.univie.ac.at/adg/schwarz/multiple.html>

binary star on the planet formation process. However, Ngo et al. (2017) found no evidence that the presence or absence of stellar companions alters the distribution of planet properties when including radial velocity systems. Observations from the redesigned *Kepler* mission, *K2*, uncovered at least two Neptune-sized circumstellar planets, K2-136 (Ciardi et al. 2018) and K2-288 (Feinstein et al. 2019), with projected binary separations ~ 40 au. Martin (2017) showed that orbital precession could be affecting the detectability of circumstellar planets through transit surveys, and observations of many more binaries are needed to identify reliable population statistics. Fortunately, the *Transiting Exoplanet Survey Satellite* (*TESS*; Ricker et al. 2015) is observing large portions of the sky; it is expected to observe $\sim 500,000$ eclipsing binaries (Sullivan et al. 2015), thereby increasing the prospects of detecting circumstellar planets in binaries.

Most studies have used the stability limit formulas developed by Holman & Wiegert (1999) to determine whether a circumstellar or circumbinary candidate within a binary system is *bone fide* and not a false positive. Holman & Wiegert (1999) note that the formulas have limitations: most notably that circular, coplanar test particles were used in its development and the expressions are valid to within 4%–11%. Pilat-Lohinger & Dvorak (2002) and Pilat-Lohinger et al. (2003) also performed a study for circumstellar planets using the Fast Lyapunov Indicator (Froeschlé et al. 1997) and explored a limited range of planets on inclined orbits. The stability of circumbinary orbits has been investigated, including the effects of mutual inclination (Doolin & Blundell 2011) and planet packing (Kratter & Shannon 2014; Quarles et al. 2018b). Those approaches have even been applied to the Pluto-Charon system (Kenyon & Bromley 2019a, 2019b), allowing for better mass estimates of the satellites. New methods and updated formulas, such as machine learning (Lam & Kipping 2018) and grid-based interpolation (Quarles et al. 2018b), have substantially reduced the uncertainty in the stability limit for circumbinary planets. We implement a similar method, proposed by Quarles et al. (2018b), to update the stability limit for circumstellar planets.

In this work, we extend the grid-based interpolation method to massive circumstellar planets, identify changes to the stability limit relative to the mutual inclination of the planet, and estimate the probability density function given the known distribution of binary stars along with a prospective critical semimajor axis ratio a_c/a_{bin} . Our numerical setup is described in Section 2, which includes our definition for stability and starting conditions. In Section 3, we determine a revised stability limit, considering circular and eccentric binaries, and accounting for a significant mutual inclination between the planetary and binary orbital planes. In addition, we investigate methods to utilize our results through interpolation maps and lookup tables. Section 4 explores more stringent conditions on the stability limit, which are due to the secular forcing of eccentricity from the stellar binary. Section 5 applies our revised stability limit to binary star population statistics and a system recently observed by *TESS*, LTT 1445ABC. Finally, our results and concluding remarks are summarized in Section 6.

2. Methods

2.1. Defining Stability and the Stability Limit

One of the defining features when expanding from the two-body (Kepler) problem to the three-body problem (TBP) is the

emergence of chaos (see details in Mudryk & Wu 2006; Musielak & Quarles 2014), or a sensitivity to initial conditions where the future state of a system is indeterminate after a sufficient time. The possible outcomes within the TBP are broadly defined as stable (i.e., the system is bounded in space and consists of three bodies for all time) or unstable (i.e., at least one body is no longer bounded in space or a collision occurs). Notice that these definitions do not explicitly include chaos—where bundles of initial conditions can be either stable or unstable, as well as chaotic. There is a transition between stable and unstable states that has been identified within astronomical systems (Lecar et al. 1992; Smith & Szebehely 1993; Goździewski et al. 2001; Pilat-Lohinger & Dvorak 2002; Cincotta et al. 2003; Cuntz et al. 2007; Eberle et al. 2008; Quarles et al. 2011; Giuppone et al. 2012; Satyal et al. 2013) using chaotic indicators similar to the Lyapunov exponent (Benettin et al. 1980; Gonczi & Froeschle 1981; Froeschlé et al. 1997; Cincotta & Simó 1999, 2000).

Due to this transition region, we must be more precise about our definitions for stability and allow for a more probabilistic consideration. Moreover, we cannot compute the evolution of a system for all time, and thus we define a given initial condition as potentially stable if the planet survives for a predefined timescale ($\sim 10^5$ yr) around its host star. Previous works (David et al. 2003; Fatuzzo et al. 2006; Quarles & Lissauer 2016) have shown that most of the initial conditions that will become unstable over longer timescales exist near mean motion resonances (MMRs) at the edge of stability; our approach excludes the resonant region, due to its dependence on the initial mean longitude of the planet. Unstable initial conditions are those that do not survive for the required timescale, either due to a collision of the planet with either of the host stars or because the distance to the host star exceeds 200 au (i.e., twice the largest binary semimajor axis considered).

Observations of planets in binaries are usually so limited that a full initial condition is not available. Rabl & Dvorak (1988) and Holman & Wiegert (1999) accounted for this by prescribing their stability criterion in terms of a set of observables that are the most readily obtained (e.g., binary mass ratio, binary eccentricity, semimajor axis ratio). The binary mass ratio $\mu (= M_B/(M_A + M_B))$ and the binary eccentricity e_{bin} can be deduced from photometric and/or radial velocity observations. The semimajor axis ratio a_p/a_{bin} can be determined if the respective orbital periods are well-determined; otherwise, projected values are typically used. Due to the long orbital periods involved and small number of observations, not many other observables are typically known. As a result, Holman & Wiegert (1999) assumed that the orbital planes of the binary and planet are aligned (i.e., $i_p = i_{\text{bin}} = \omega_p = \Omega_p = \omega_{\text{bin}} = \Omega_{\text{bin}} = 0^\circ$) and the planetary orbit is initially circular (i.e., $e_p = 0$). Additionally, the restricted TBP was implemented, where a *massless test particle* was used for the planet, as a matter of numerical efficiency.

A combination of parameters (μ , e_{bin} , and a_p/a_{bin}) are numerically evolved for eight equally spaced planetary phase angles, and if all eight of the trials are deemed stable, a critical semimajor axis a_c is determined. Most of our simulations follow this general approach, except we use an Earth-mass particle that gravitationally interacts with the binary and evaluate 91 initial planetary phase angles so that we can investigate the probabilistic transition region between stable and unstable orbits. The stability limit a_c is defined in our

Table 1
Range of Initial Conditions Used in Our Simulations

Parameter	Range	Step
μ	0.01–0.99	0.01
e_{bin}	0.00–0.80	0.01
a_p/a_{bin}	0.010–0.800	0.001
i_p	0° – 180°	30°
λ_p	0° – 180°	2°

Note. The range of mass ratio μ also includes two additional extreme values: 0.001 and 0.999. The range of planetary inclination i_p is restricted to 0° , 30° , 45° , and 180° for our simulations with eccentric binaries.

analysis as the largest semimajor axis ratio a_p/a_{bin} , where all 91 initial phase angles ($0^\circ \leq \lambda_p \leq 180^\circ$) survive up to our predefined timescale.

2.2. Setup for Numerical Simulations

The numerical simulations in our study use a integration package that has been modified such that the orbits of planets in binaries are efficiently evaluated (`MERCURY6`; Chambers et al. 2002). This well-established code was developed for planet formation simulations within α Centauri AB (Quintana et al. 2002), where a hybrid scheme allows for switching between a symplectic integration method (i.e., Wisdom–Holman splitting (Wisdom & Holman 1991, 1992)) and an adaptive method (e.g., Bulirsch–Stoer (Press et al. 1993)). We check a subset of our runs using a newer N -body code, REBOUND, with the IAS15 integrator (Rein & Liu 2012; Rein & Spiegel 2015) to ensure the accuracy of our results.

We set up our simulations starting from a set of unitless parameters (μ , e_{bin} , and a_p/a_{bin}), which allows for scalability of our results to many different dynamical systems. Table 1 gives the range of these parameters, along with the range of inclination and mean longitudes for defining an orbit. The total mass of the binary is equal to one solar mass ($M_A + M_B = 1 M_\odot$), and the individual stellar masses are determined via $\mu (= M_B/(M_A + M_B))$. The initial planetary semimajor axis a_p is 1 au and the initial value of the semimajor axis ratio is used to determine the appropriate binary semimajor axis (~ 1 – 100 au). The initial phase of the binary begins at periastron ($\lambda_{\text{bin}} = 0^\circ$), which lies on the positive x -axis ($\omega_{\text{bin}} = 0^\circ$) within the orbital plane of the binary. All of our simulations use the binary orbital plane as a reference ($i_{\text{bin}} = \Omega_{\text{bin}} = 0^\circ$), where the initial planetary inclination i_p is the relative angle between the planetary and binary orbital planes. Moreover, these orbital planes begin nodally aligned ($\Omega_p = \Omega_{\text{bin}}$).

The accuracy of our simulations is controlled by choosing a time step that is 5% of the planetary orbital period T_p ($\propto (1 - \mu)^{-1/2}$). Stability studies of α Cen AB (Wiegert & Holman 1997; Quarles & Lissauer 2016) have shown that the region of stability does not change appreciably until i_p is greater than 40° , and the extent of stability increases for retrograde orbits. There is an intermediate region ($40^\circ \gtrsim i_p \gtrsim 140^\circ$) where the Lidov–Kozai (LK) mechanism (Kozai 1962; Lidov 1962) drives large eccentricity oscillations that can reduce stability zones unless the planet and binary are apsidally misaligned by 90° (Giuppone & Correia 2017). We probe a wide range of planetary inclinations (0° , 30° , 60° , 85° , 95° , 120° , 150° , and 180°) for circular binaries, and then we limit our investigation of

eccentric binaries to four planetary inclinations: 0° , 30° , 45° , and 180° . The mass ratio μ is varied uniformly in steps of 0.01 from 0.01 to 0.99, where we also evaluate the special cases of 0.001 and 0.999. The binary eccentricity e_{bin} is sampled in 0.01 steps from 0 to 0.8, while the semimajor axis ratio a_p/a_{bin} ranges from 0.01 to 0.8 in steps of 0.001. While the initial phase of the binary remains fixed ($\lambda_{\text{bin}} = 0^\circ$), the mean longitude of the planet is varied in 2° steps from 0° to 180° .

2.3. Symmetries in the Parameter Space

The range of parameters that we explore is quite broad—and necessarily so, in order to provide the most general results. Our previous study of circumbinary planets (Quarles et al. 2018b) exploited a symmetry in the initial mean longitude, and allowed for the computations to be performed efficiently. To evaluate whether similar symmetries exist, we find the maximum eccentricity a planet attains when beginning from a circular orbit. Figure 1 illustrates the maximum eccentricity that a coplanar planet attains for stable configurations as a function of the initial semimajor axis ratio a_p/a_{bin} and mean longitude λ_p , where the white regions represent initial conditions that are unstable on a 500,000 yr timescale. The panels are labeled to show the mass ratio μ and stability limit a_c determined. As the mass ratio increases (top to bottom), the stability limit a_c decreases and the maximum eccentricity increases by an order of magnitude. Additionally, the first column shows a symmetry in the mean longitude that appears more strongly with increasing μ . The growth of the maximum eccentricity is more pronounced when the binary eccentricity e_{bin} increases (left to right). Indeed, these trends are known from secular studies (Andrade-Ines et al. 2016; Andrade-Ines & Eggl 2017, and references therein), and further indicates the accuracy of our numerical simulations. These trends justify our numerical setup (see Section 2.2) and particular restrictions in mean longitude when surveying the full parameter space.

Other dynamical effects, such as the Lidov–Kozai (LK) mechanism (Kozai 1962; Lidov 1962), can arise when considering inclined orbits and affect how much we can exploit particular symmetries. In Figure 2, we perform similar simulations as in Figure 1, but for inclined orbits with a constant mass ratio ($\mu = 0.1$). The planetary inclination i_p and determined stability limit a_c are given as tuples in the lower left of each panel. The difference between a planet inclined by 30° relative to the coplanar case is relatively minor, where variations occur mainly at large semimajor axis ratio that depend on the initial mean longitude. When the planetary inclination is increased to 45° , the stability limit a_c decreases more substantially relative to the coplanar case and the typical maximum eccentricity is ~ 0.5 across most semimajor axis ratios. Finally, our retrograde ($i_p = 180^\circ$) runs demonstrate a $\sim 25\%$ increase in the stability limit a_c relative to the respective coplanar runs. This is roughly what one would expect from previous studies of the restricted TBP, where stable particles fill a larger portion of the Hill radius (Henon 1970). Overall, Figures 1 and 2 demonstrate that the range of mean longitude required to determine the stability limit can be reduced to 0 – 180° independent of the initial planetary inclination i_p , and it is possible that a separate condition can be placed on the maximum eccentricity, where $e_{\text{max}} \lesssim 0.5$.

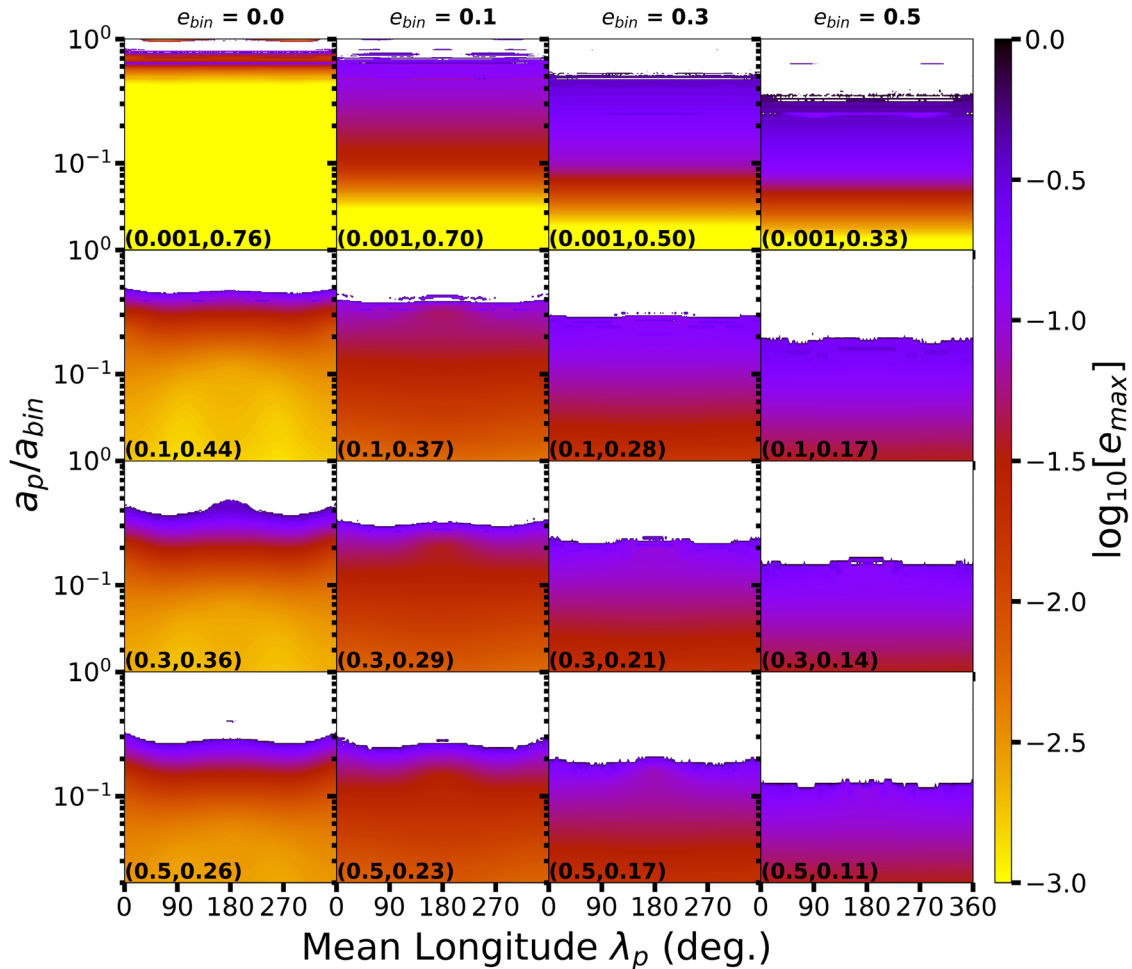


Figure 1. The maximum planetary eccentricity attained (color-coded on a logarithmic scale) for coplanar initial conditions that survive for 5×10^5 yr of simulation time over a range of initial semimajor axis ratios a_p/a_{bin} and mean longitudes λ_p . Each panel contains a label (μ, a_c) indicating the host binary mass ratio and the critical semimajor axis ratio determined for each binary configuration, respectively. Note the mirror symmetry about $\lambda_p = 180^\circ$.

3. Revised Stability Limit

To meaningfully revise the previous determination of stability limit a_c for circumstellar planets in binaries (Holman & Wiegert 1999), we perform a large number of numerical simulations⁶ (~ 700 million in total) that report the lifetime of a planet and the maximum eccentricity attained for each set of initial conditions. We use four input parameters $(\mu, e_{\text{bin}}, a_p/a_{\text{bin}}, \lambda_p)$ that relate to the most easily obtained observables, and iterate this process over a range of planetary inclinations (see Section 2.2) that are representative of the dynamical interactions affecting the stability limit. In this section, our analysis is divided into three parts: the case of circular binaries ($e_{\text{bin}} = 0$), a comparison to previous results from Holman & Wiegert (1999) with elliptical binaries ($e_{\text{bin}} \leq 0.8$), and the interpolation maps across each planetary inclination.

3.1. Circular Binaries

One of the oldest problems studied within orbital dynamics is the circular restricted three-body problem (CRTBP), where the two more massive primaries begin on circular orbits and the third body is not massive enough to substantially alter the orbit

of the primaries; see Musielak & Quarles (2014) for a review. Due to the restriction on the binary orbit’s eccentricity, an integral arises that reduces some of the complexity. The solution to the integral, or Jacobi constant C_J in the CRTBP, provides a natural means to orient our analysis. The so-called zero velocity contour (ZVC) for a given mass ratio μ and semimajor axis ratio a_p/a_{bin} describes a topological boundary that limits the trajectory of a planet and can be related to the Jacobi constant (Eberle et al. 2008).

We use this formalism to explore the changes in the trajectory for a single initial condition ($\mu = 0.3$, $a_p/a_{\text{bin}} = 0.369$, and $\lambda_p = 180^\circ$) with respect to a changing planetary inclination. Figure 3 shows each trajectory over one orbit of the binary using inertial or static coordinates (left column) and rotated coordinates (right column), where the rotation rate is equal to the binary mean motion. The nominal location of the $N:1$ MMRs, in terms of semimajor axis ratio, is $a_p/a_{\text{bin}} = ((1 - \mu)/N^2)^{1/3}$, which places the initial condition between the 4:1 and 3:1 MMRs. For the coplanar case in Figure 3(a), we trace the trajectory of the planet to nearly complete three orbits within one binary orbit. This results in a quasi-periodicity for the trajectory in the rotated coordinates (Figure 3(b)) and is bounded by the ZVC. When the planet is inclined by 30° in Figure 3(c), it follows a similar trajectory within a tilted plane and small differences appear due to the

⁶ The results of our simulations are publicly available at doi:10.5281/zenodo.3579202 as a series of compressed tar archives.

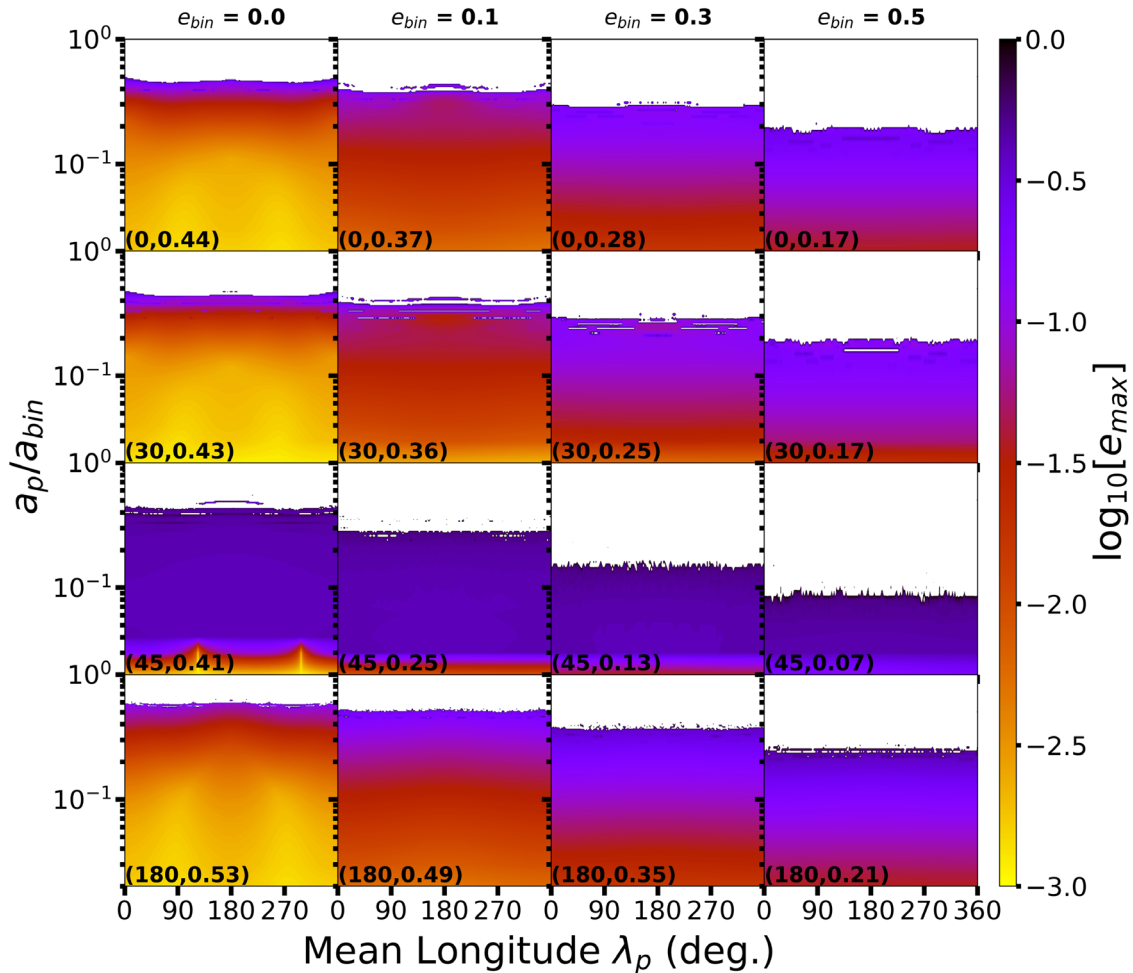


Figure 2. Similar to Figure 1, but the mass ratio is constant ($\mu = 0.1$) and the planetary inclination is varied. Each panel contains a label (i_p, a_c) indicating the planetary inclination and the critical semimajor axis ratio, respectively. Note the mirror symmetry about $\lambda_p = 180^\circ$ remains for inclined orbits.

projection onto the X - Y plane. The planetary orbit is more eccentric (not just in appearance due to projection) once the inclination is increased to 30° in Figure 3(e). A retrograde ($i_p = 180^\circ$) planet executes the most regular trajectory, where almost five orbits are now completed within a single binary orbit (Figure 3(g)) and the trajectory is periodic in rotated coordinates (Figure 3(h)). From these example trajectories, we expect that the stability results for planetary inclinations up to 30° to not differ too much from those determine for a coplanar orbit. The increased eccentricity from the Lidov-Kozai mechanism will introduce a dependence on the initial mean longitude, due to apsidal precession, and retrograde orbits will be stable to significantly larger semimajor axis ratios.

In the CRTBP, some regions of the parameter space are more chaotic; these appear once the ZVC opens at the Lagrange point L_1 , which lies between the stars (Quarles et al. 2011). Additional chaos can arise when the other collinear Lagrange points no longer lie within the forbidden region, due to changes in the mass ratio μ or the semimajor axis ratio a_p/a_{bin} . The origin of chaos in the CRTBP lies in the overlap of the $N:1$ MMRs with the binary, once the planetary eccentricity is substantially excited by a resonance (Murray & Dermott 1999; Mardling 2008). We take a wide view of the possible initial conditions (μ , a_p/a_{bin} , and λ_p) to produce probabilistic maps for a range of planetary inclinations in Figure 4. The probability for stability is calculated simply as the percentage

of simulations (out of 91 values for λ_p) that survive for 500,000 yr for a given mass ratio and semimajor axis ratio. As a result, we identify regions that are stable (black), unstable (white), and quasi-stable (light or dark gray). The quasi-stable region is split into two regimes where either 1–18 trials survive (1%–20%; light gray) or 19–90 trials survive (20%–99%; dark gray) to delineate between chaotic zones and possible resonant islands that strongly depend on λ_p . In Figure 4, each panel also marks the critical boundaries (red curves) for which the ZVC opens for a collinear Lagrange point (L_1 , L_2 , or L_3) as detailed in Eberle et al. (2008) using the respective Jacobi constant (C_1 , C_2 , or C_3).

Eberle et al. (2008) and Quarles et al. (2011) explored the coplanar case (Figure 4(a)) in detail using the Jacobi constant and maximum Lyapunov component, respectively, for planets that orbit the more massive primary ($\mu \leq 0.5$). However, Figure 4(a) shows that using the Jacobi constant C_1 as a stability criterion agrees well for all μ and only a few stable (black) regions exist to the right of the solid red curve, C_1 . Between the curves for C_1 and C_3 , there are initial conditions that can be stable depending on the initial mean longitude due to MMRs (Morais & Giuppone 2012; Morais & Namouni 2013), as indicated by the quasi-stable (light and dark gray) region, and Quarles et al. (2011) identified this regime as chaotic using the maximum Lyapunov exponent. All of the initial values to the right of C_3 (dashed red curve) are

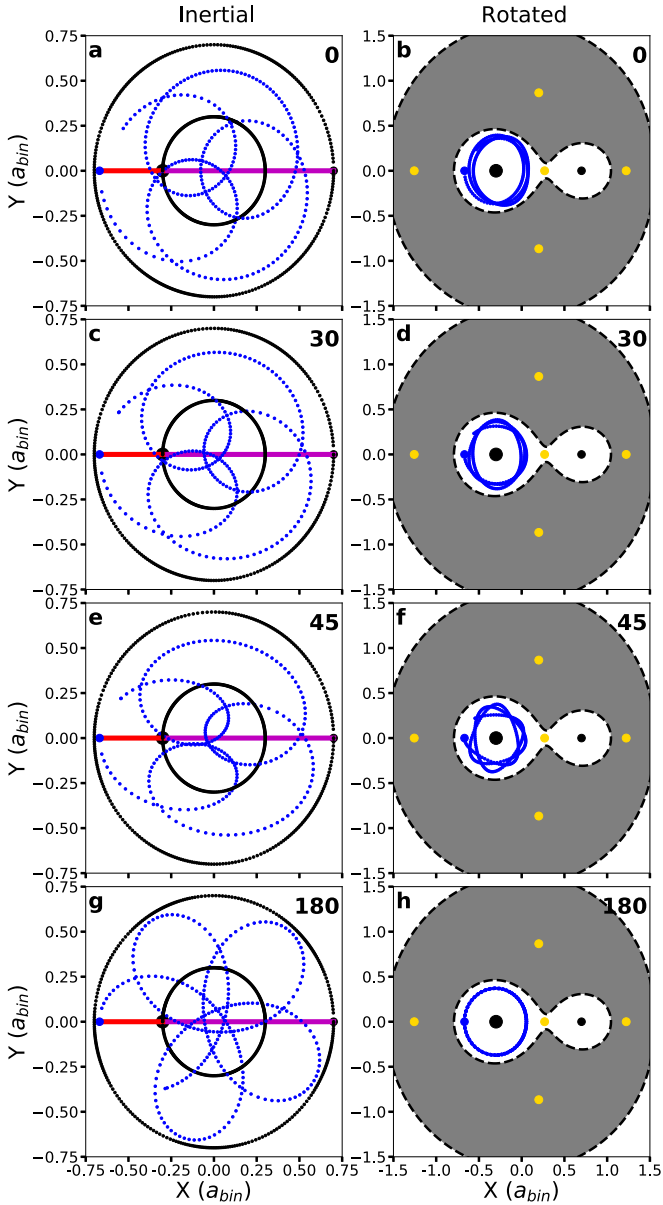


Figure 3. The trajectories in the X – Y plane for a three body system ($\mu = 0.3$, $a_p/a_{\text{bin}} = 0.369$, and $\lambda_p = 180^\circ$) in inertial (left) and rotated (right) coordinates for a range of mutual inclinations in degrees (top right). The initial distance of the planet to the host star is marked by a red line, where the binary semimajor axis is indicated by a magenta line. The trajectory of the planet over one orbit of the more massive primary is given in each coordinate system, where the planet begins inclined to the X – Y plane as indicated in the top right corner. Gold points in the right column correspond to the Lagrange points. Black dashed contours denote the boundaries of zero velocity in the rotated coordinates and the forbidden region is shaded gray. Note the difference in scale between the two columns.

unstable due to large excitations of the planetary eccentricity by the perturbing star and the opening of all the collinear Lagrange points in the ZVC.

After the planet is inclined 30° relative to the binary orbit (Figure 4(b)), the stable (black) region does not change much. Panels (c) and (d) of Figure 4 illustrate significant differences from the coplanar cases due to the LK mechanism, where a large periodic eccentricity oscillation occurs that erodes much of the parameter space between the C_1 and C_3 curves. The stable regime for Figure 4(d) lies significantly below the C_1

curve, demonstrating the effectiveness of the LK mechanism. Some resonant regions (i.e., $N:1$ MMRs) can remain stable for longer periods, but must maintain a special configuration (e.g., similar to Pluto’s 3:2 MMR with Neptune).

Panels (e)–(h) of Figure 4 show how the stability regions vary for retrograde orbits ($i_p^{\text{retro}} = 180^\circ - i_p$), where the stable retrograde initial conditions (black) in Figure 4(e) represent a much larger fraction of the parameter space and do not agree with the Jacobi constant stability criterion from Eberle et al. (2008). The extent of the quasi-stable regime (light or dark gray) also increases, but it reaches a limit at the 3:2 MMR with the binary orbit. Figure 4(f) can be largely constrained with the Jacobi constant, and appears very similar in extent to Figure 4(b). Panels (g) and (h) in Figure 4 are similar to their prograde counterparts (Figure 4(c) and (d)), but the stabilizing effects from starting in retrograde increase the extent of the quasi-stable region at high μ and a_p/a_{bin} .

Another special circumstance can arise when the planet begins with a significant orbital velocity out of the binary plane so that the Coriolis force is minimized. In this scenario, the initial orbital velocity is calculated assuming the lower-mass star is the host (i.e., high μ), but the high semimajor axis ratio a_p/a_{bin} starts the planet within the Hill sphere of the more massive star. As a result, the planet can be captured into $N:1$ MMRs by the primary. Although this setup is allowed (i.e., no physical laws broken), it could be very unlikely to occur within known pathways for planet formation, but we highlight it for completeness. Figure 5 illustrates the evolution of a particular initial condition in rotated coordinates that can lead to this type of capture, where the planet begins either coplanar (Figure 5(a)) or highly inclined (Figure 5(c)). To confirm a capture into the 3:1 MMR, we plot the evolution of the resonance angle $\phi_{3:1}$, where there are points in the coplanar case (Figure 5(b)) that are ill-defined (i.e., vertical jumps) and the highly inclined simulation (Figure 5(d)) shows libration.

Even in the simplified case of the CRTBP, there is not a simple expression to define the likelihood that a planetary orbit will be stable. The most straightforward prescription to estimate stability is N -body simulations on a case-by-case basis, but this process can be greatly expedited or avoided using our results. For a nearly *coplanar* planet within a circular binary (e.g., transiting an eclipsing binary), the stability limit can be estimated using the Jacobi constant at the first Lagrange point C_1 . We provide an algorithm to determine this curve as follows:

1. Choose a value of μ from a list.
2. Approximate through a power series or numerically determine the Lagrange point L_1 using a given μ and a root finding function.
3. Use the location of L_1 to determine the Jacobi constant C_1 using the equation for the zero velocity surface ($2U = C_j$; see Chap. 3 of Murray & Dermott 1999)
4. Use the value of C_1 from (3) and numerically solve Equation (14) from Eberle et al. (2008) using a root finding function.
5. Go back to (1), until the end of the list is reached.

Table 2 lists values for the semimajor axis ratio and mass ratio, where openings of the ZVC occur at L_1 or L_3 using the above algorithm, and these values correspond to the red curves (C_1 or C_3 , respectively) in Figure 4. For a moderately *inclined* planet within a binary, similar curves provide a good approximation

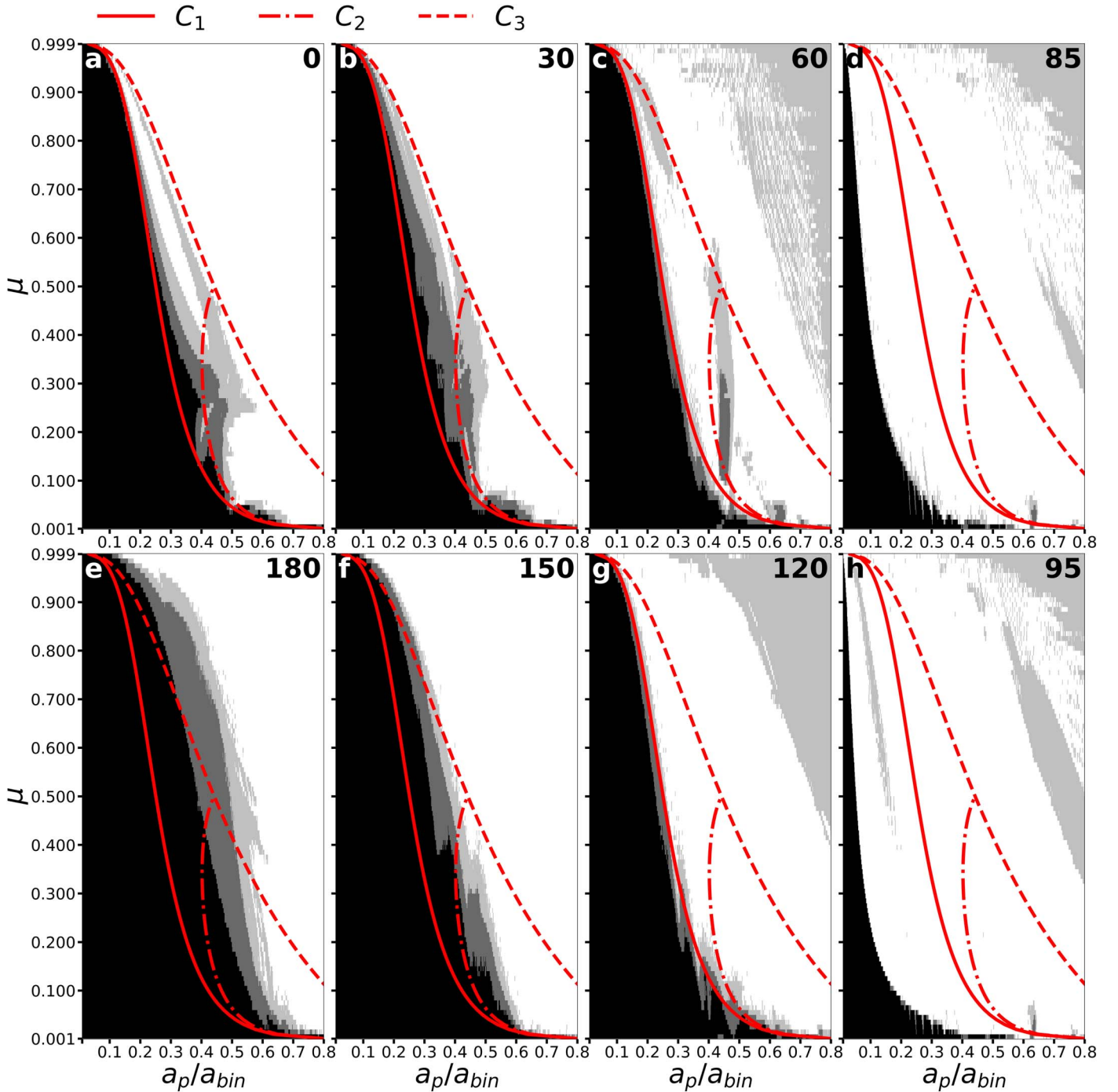


Figure 4. The stability regions within the CRTBP for a range of initial values in the mass ratio μ and semimajor axis ratio a_p/a_{bin} , considering a potentially inclined planet with the respective inclination in the top right corner. Black cells indicate that all 91 trials survive for the entire 500,000 yr of the simulation (i.e., stable), where the dark or light gray cells mark those when either 20%–99% or 1%–19% of the trials survive, respectively. White cells denote initial conditions, where none of the trials survive (i.e., unstable). Red curves correspond to openings in the zero velocity curve at each Lagrange point (Eberle et al. 2008).

for the stability limit, but a coplanar retrograde orbit can significantly expand the stability limit as shown by C_1^{retro} . Finally, we provide Python tools on GitHub to query the data set represented in Figure 4, and there is a routine that returns the probability for stability through grid interpolation for a given combination of μ and a_p/a_{bin} .

3.2. Eccentric Binaries

Planets orbiting a single star of a circular binary represent only a subset of all the possibilities—and thus, we extend our

method to investigate binary systems with a significant eccentricity ($e_{bin} \leq 0.8$). This extra dimension expands the volume of our parameter space by almost two orders of magnitude, and thus we perform our numerical simulations with computational efficiency in mind. In Section 3.1, we explore eight different mutual inclinations because the eccentricity forcing on the planet is mainly due to MMRs. For eccentric binaries, we limit our investigation to only four mutual inclinations ($i_p = 30^\circ, 45^\circ, \text{ and } 180^\circ$), as the LK mechanism greatly reduces the stability limit within the

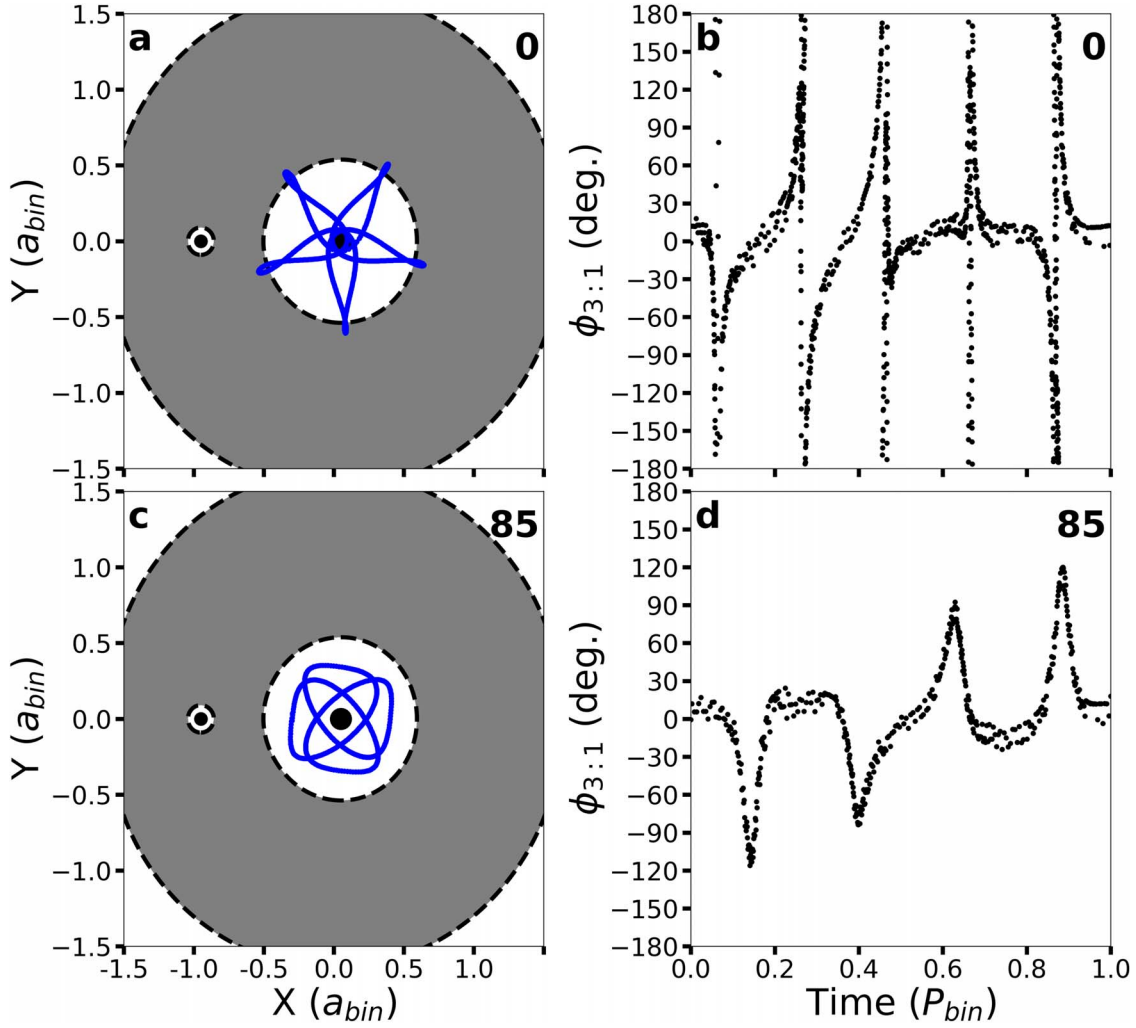


Figure 5. The trajectory of a coplanar or highly inclined planet in rotated coordinates over a single orbit of the binary beginning with $a_p/a_{\text{bin}} = 0.78$, a host binary with $\mu = 0.95$, and an initial mean anomaly $MA = 33^\circ$. Panel (a) differs from panel (c) in the starting planetary inclination (indicated in upper right), which manifests in a difference in the strength of the Coriolis force. The starting condition lies within the Hill sphere of the more massive star (near origin), and can result in the possible capture in the 3:1 MMR. Panels (b) and (d) illustrate the evolution of the resonance angle for the 3:1 MMR, $\phi_{3:1} = 3\lambda_{\text{bin}} - \lambda_p - 2\varpi_{\text{bin}}$.

40–140° range of inclination (Quarles & Lissauer 2016; Quarles et al. 2018a).

Our coplanar simulations ($i_p = 0^\circ$) use the uniform stepping described in Section 2.2 to determine the stability boundary a_c . To make the exploration of the inclined cases more efficient, we use the method of Lam & Kipping (2018), where they focused on a range in semimajor axis ratio (i.e., window) that would most likely contain the stability limit. To do this, we use the results from the coplanar runs to determine an appropriate trial window for the other inclined cases ($i_p = 30^\circ, 45^\circ$, and 180°). We then numerically investigate for longer timescales (500,000 yr) using semimajor axis ratios within $0.5a_c^0 - 1.5a_c^0$, where a_c^0 is the stability limit in the respective prograde, coplanar simulation. If all the simulations in this range $0.5a_c^0 - 1.5a_c^0$ are unstable, then we explore a range of smaller semimajor axis ratios ($0.001 \leq a_p/a_{\text{bin}} \leq 0.5a_c^0$). This procedure was sufficient to cover regions of parameter space that we expect to either be truncated (e.g., Lidov–Kozai mechanism for $i_p = 45^\circ$) or expanded (e.g., retrograde orbits for $i_p = 180^\circ$).

Following Holman & Wiegert (1999), we take these results and compare to previous studies (Rabl & Dvorak 1988) that

prescribe a stability limit for equal mass stars ($\mu = 0.5$). Figure 6 illustrates how our results compare for the special case of equal mass stars with a coplanar planet, the range of stability for two regimes of μ (red and blue), and the changes to the median stability limit within each regime for each planetary inclination. Rabl & Dvorak (1988) performed simulations for only 300 binary periods and explored up to $e_{\text{bin}} = 0.6$. Thus, we expect for deviations to appear for high binary eccentricities ($0.6 \leq e_{\text{bin}} \leq 0.8$ where the expression from Rabl & Dvorak (1988) is extrapolated as seen in Figure 6(a). There is also a small difference between the curve from Holman & Wiegert (1999) (black dashed) and our results (solid gray) in the high binary eccentricity region, as well as in the $e_{\text{bin}} \leq 0.1$ region. These differences are due to the factor of 10 increase in sampling that we perform, and amount to slight changes in the stability limit for a coplanar planet. The shaded regions (red and blue) in Figure 6(a) demonstrate the extent to which the stability limit can vary as a function of μ , where $\mu = 0.01$ follows the upper red boundary and $\mu = 0.99$ is much flatter along the lower blue boundary. As in the case for the CRTBP, we can see that the stability limit is not symmetric about the equal mass case.

Table 2
Stability Limits in the CRTBP Using the Mass Ratio and Jacobi Constant Criterion

μ	C_1	C_3	C_1^{retro}
0.001	0.7988	0.9978	0.780
0.01	0.6368	0.9785	0.689
0.05	0.4906	0.9012	0.582
0.10	0.4230	0.8201	0.549
0.15	0.3825	0.7515	0.519
0.20	0.3533	0.6921	0.496
0.25	0.3301	0.6399	0.475
0.30	0.3107	0.5932	0.455
0.35	0.2937	0.5509	0.438
0.40	0.2784	0.5120	0.422
0.45	0.2644	0.4760	0.405
0.50	0.2511	0.4421	0.389
0.55	0.2385	0.4100	0.373
0.60	0.2261	0.3792	0.357
0.65	0.2137	0.3492	0.340
0.70	0.2011	0.3195	0.322
0.75	0.1880	0.2898	0.302
0.80	0.1738	0.2592	0.281
0.85	0.1579	0.2266	0.256
0.90	0.1387	0.1899	0.225
0.95	0.1119	0.1436	0.180
0.99	0.0682	0.0790	0.107
0.999	0.0329	0.0353	0.048

Note. Semimajor axis ratio a_p/a_{bin} of the stability limit for a given mass ratio μ , and using the Jacobi constant C_1 and C_3 as a stability criterion at the Lagrange points L_1 and L_3 , respectively. Here, C_1^{retro} marks the numerically determined stability boundary for retrograde orbits ($i_p = 180^\circ$), due to a limitation of the Jacobi constant criterion, where the uncertainties in these values are 0.001.

The planetary inclination also plays a role in determining the stability limit a_c , where Figure 6(b) shows these differences through quadratic fits to the median stability limit for each e_{bin} . The $i_p = 0^\circ$ (solid) and $i_p = 30^\circ$ (dashed) curves are nearly identical in Figure 6(b), and there is not a strong dependence on μ when split into the two regimes (red and blue). As a result, the stability limit for coplanar planets will be similar enough, in most cases, to be valid up to $\sim 40^\circ$, until the Lidov–Kozai mechanism becomes active. The same will be true for retrograde planetary inclinations ($140^\circ \leq i_p < 180^\circ$) relative to the exactly retrograde case ($i_p = 180^\circ$). Sufficiently inclined planets ($i_p = 45^\circ$; dashed–dotted in Figure 6(b)) where the Lidov–Kozai mechanism is active have a lower median stability limit, due to eccentricity excitation, and it is largely independent of μ . On the other hand, planets in retrograde orbits (dotted in Figure 6(b)) have a larger median stability limit.

Table 3 provides coefficients and uncertainties for the quadratic fitting formula ($a_c/a_{\text{bin}} = c_1 + c_2 e_{\text{bin}} + c_3 e_{\text{bin}}^2$) from Rabl & Dvorak (1988), Holman & Wiegert (1999), and using the stability limits determined through our simulations. The difference between our coplanar results ($i_p = 0^\circ$) and the previous studies is that we break the fitting formula into two regimes for μ , as motivated by the CRTBP and Figure 6. If we find the average value for each coefficient ($c_1 - c_3$), then our results are consistent with the previous works. Our c_1 and c_2 coefficients for $i_p = 30^\circ$ are similar to our coplanar coefficients. The coefficients for the $i_p = 45^\circ$ fitting formula depend more strongly on the binary eccentricity due to the

Lidov–Kozai mechanism. The coefficients for the retrograde fitting formulas are larger than the coplanar, prograde formulas by more than 30%. Moreover, each set of coefficients reveal that the stability limit could be up to two times bigger for planets that orbit the more massive primary over the less massive secondary star.

An accurate and reliable fitting formula should include a dependence on the mass ratio μ , given the asymmetries we have described in the CRTBP and in Figure 6. Holman & Wiegert (1999) assumed that the stability limit depends linearly on μ and quadratically for e_{bin} . We follow the same prescription and provide updated values for the coefficients $c_1 - c_6$, using our much larger data set in Table 4 along with the previous values from Holman & Wiegert (1999) for comparison. Moreover, coefficients are listed for inclined planets ($i_p = 30^\circ$, 45° , and 180°), where we see that the coefficients for the coplanar and 30° formulas are similar. When the planet is initially inclined to 45° , the $c_3 - c_6$ terms dominate due to the strong dependence on e_{bin} from the Lidov–Kozai mechanism. The c_1 , c_3 , and c_5 coefficients for retrograde are larger than the respective coefficients for $i_p = 0^\circ$ formula, which indicates that retrograde stability depends more strongly on e_{bin} , due to a lower magnitude forcing on the planet from the stellar companion (Henon 1970).

3.3. Interpolation Maps and Lookup Tables

The fitting formulas in Section 3.2 are dependent on the quality and breadth of the numerical simulations that underlie their derivation. They are reliable in characterizing a population of exoplanets, but they can also be inaccurate when describing particular systems. For instance, we can compare the case when $e_{\text{bin}} = 0$ in Table 4 to the results in Table 2. The estimate for the critical semimajor axis a_c from Holman & Wiegert (1999) and our own newly updated estimation is different by more than 10% for $\mu < 0.05$. As a result, we suggest a different approach using a lookup table or interpolation map that relies less on statistical averaging, which occurs in deriving a single fitting formula.

Figure 7 shows⁷ the critical semimajor axis ratio a_c/a_{bin} (color-coded) over the full range of mass ratio μ and binary eccentricity e_{bin} . Table 4 shows only small differences in the fitting formulas for $i_p = 0^\circ$ and $i_p = 30^\circ$, where this trend is visually apparent in Figure 7(a) and (b). In addition, panels (a) and (b) illustrate the asymmetry of the stability limit with respect to the mass ratio μ , where for $\mu > 0.5$ the typical value is $a_c/a_{\text{bin}} \lesssim 0.2$. As a result, we find the volume for a stable planet for the primary star to host a nearly planar ($i_p \leq 30^\circ$) planet in a low mass ratio ($\mu < 0.3$) binary to be typically two times larger than for the lower-mass secondary ($\mu > 0.7$). The propensity for stable orbits is substantially reduced for a more inclined ($i_p = 45^\circ$) planet when $e_{\text{bin}} \gtrsim 0.2$ and the critical semimajor axis becomes more symmetric about $\mu = 0.5$ (Figure 7(c)). A retrograde planet (Figure 7(d)) can be stable to much larger semimajor axis ratios and for a larger fraction of binary parameters (μ and e_{bin}), which has been shown to some degree in several other investigations (Henon 1970; Benest 1988b; Wiegert & Holman 1997; Quarles & Lissauer 2016).

⁷ The data for these maps are available on [GitHub](#), along with an example Python script that interpolates between grid values.

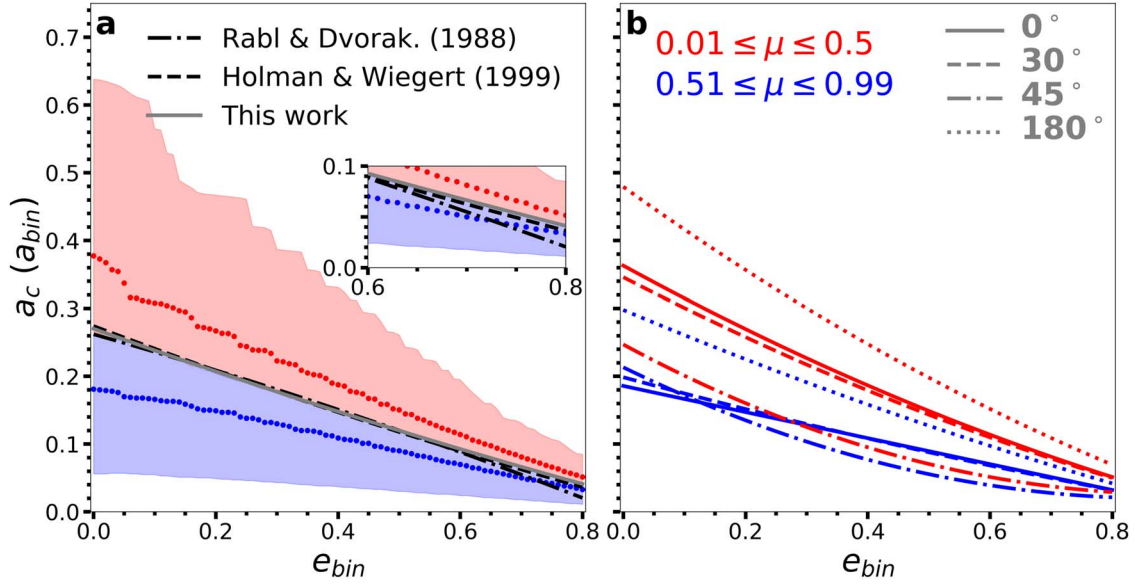


Figure 6. Critical semimajor axis a_c as a function of the binary eccentricity e_{bin} for a planet orbiting either the more (red) or the less (blue) massive star. Black curves in panel (a) illustrate the previous results for $\mu = 0.5$, where our results are given by the solid gray curve. The inset shows a magnified view for high binary eccentricity ($0.6 \leq e_{bin} \leq 0.8$), where the black and gray curves no longer overlap. The median values for a_c (color-coded points) are shown in panel (a), where the color-coded area signifies the full range with respect to each domain. The curves in panel (b) demonstrate the least squares best fit for the median a_c as a function of each planetary inclination.

Table 3
Critical Semimajor Axis as a Function of the Binary Eccentricity e_{bin}

	i_p	$c_1 \pm \sigma_1$	$c_2 \pm \sigma_2$	$c_3 \pm \sigma_3$
$0.1 \leq \mu \leq 0.9^\dagger$	0°	0.262 ± 0.006	-0.254 ± 0.017	0.060 ± 0.027
$0.1 \leq \mu \leq 0.9^*$	0°	0.274 ± 0.008	-0.338 ± 0.045	0.051 ± 0.055
$0.01 \leq \mu \leq 0.5$	0°	0.363 ± 0.001	-0.492 ± 0.006	0.129 ± 0.005
$0.51 \leq \mu \leq 0.99$	0°	0.186 ± 0.001	-0.193 ± 0.003	0.001 ± 0.003
$0.01 \leq \mu \leq 0.5$	30°	0.346 ± 0.002	-0.464 ± 0.006	0.117 ± 0.005
$0.51 \leq \mu \leq 0.99$	30°	0.198 ± 0.001	-0.243 ± 0.002	0.043 ± 0.002
$0.01 \leq \mu \leq 0.5$	45°	0.247 ± 0.005	-0.487 ± 0.018	0.268 ± 0.016
$0.51 \leq \mu \leq 0.99$	45°	0.213 ± 0.002	-0.441 ± 0.009	0.252 ± 0.008
$0.01 \leq \mu \leq 0.5$	180°	0.479 ± 0.002	-0.647 ± 0.008	0.168 ± 0.008
$0.51 \leq \mu \leq 0.99$	180°	0.298 ± 0.001	-0.378 ± 0.006	0.072 ± 0.006

Note. The listed coefficients ($c_1 - c_3$ and uncertainties ($\sigma_1 - \sigma_3$) from † Rabl & Dvorak (1988) and * Holman & Wiegert (1999) use a quadratic fitting function, $a_c/a_{bin} = c_1 + c_2 e_{bin} + c_3 e_{bin}^2$. We use the same function in this work, but we split it between two domains in μ for each planetary inclination i_p .

Table 4
Coefficients for the Critical Semimajor Axis

	i_p	$c_1 \pm \sigma_1$	$c_2 \pm \sigma_2$	$c_3 \pm \sigma_3$	$c_4 \pm \sigma_4$	$c_5 \pm \sigma_5$	$c_6 \pm \sigma_6$
Previous Work*	0°	0.464 ± 0.006	-0.380 ± 0.010	-0.631 ± 0.034	0.586 ± 0.061	0.650 ± 0.041	-0.198 ± 0.074
This work	0°	0.501 ± 0.002	-0.435 ± 0.003	-0.668 ± 0.009	0.644 ± 0.015	0.152 ± 0.011	-0.196 ± 0.019
This work	30°	0.485 ± 0.002	-0.405 ± 0.003	-0.684 ± 0.009	0.603 ± 0.015	0.190 ± 0.011	-0.182 ± 0.019
This work	45°	0.428 ± 0.002	-0.318 ± 0.003	-1.128 ± 0.011	0.987 ± 0.020	0.839 ± 0.014	-0.825 ± 0.024
This work	180°	0.617 ± 0.001	-0.457 ± 0.002	-0.787 ± 0.008	0.586 ± 0.014	0.163 ± 0.010	-0.128 ± 0.017

Note. The coefficients ($c_1 - c_6$) and uncertainties ($\sigma_1 - \sigma_6$) from * Holman & Wiegert (1999) are listed using the fitting formula, $a_c/a_{bin} = c_1 + c_2 \mu + c_3 e_{bin} + c_4 \mu e_{bin} + c_5 e_{bin}^2 + c_6 \mu e_{bin}^2$. We use the same function in this work, but also fit for a range of planetary inclination i_p .

4. More Stringent Stability Criteria

It is possible to devise a more stringent stability criterion that depends on more parameters. Part of the motivation for Holman & Wiegert (1999) to use the binary mass ratio μ and

eccentricity e_{bin} was that these parameters are relatively easy to determine through an adequate number of observations through radial velocity or photometric surveys. However, the *Kepler* era

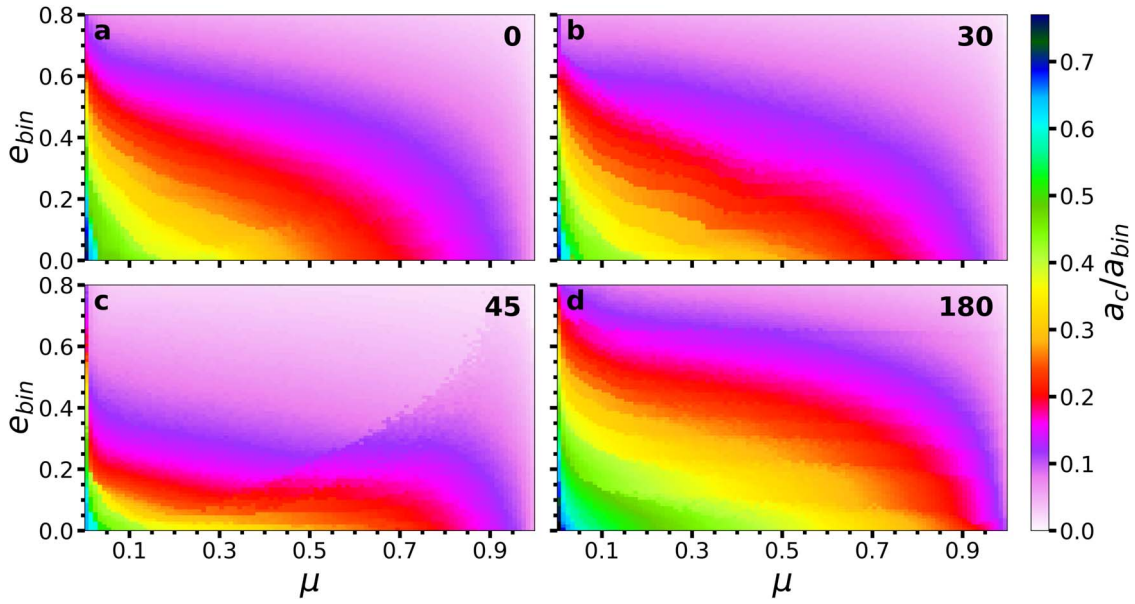


Figure 7. Critical semimajor axis a_c (color-coded) as a function of the binary eccentricity e_{bin} and the mass ratio μ . The initial planetary inclination i_p is denoted in each panel in the upper right.

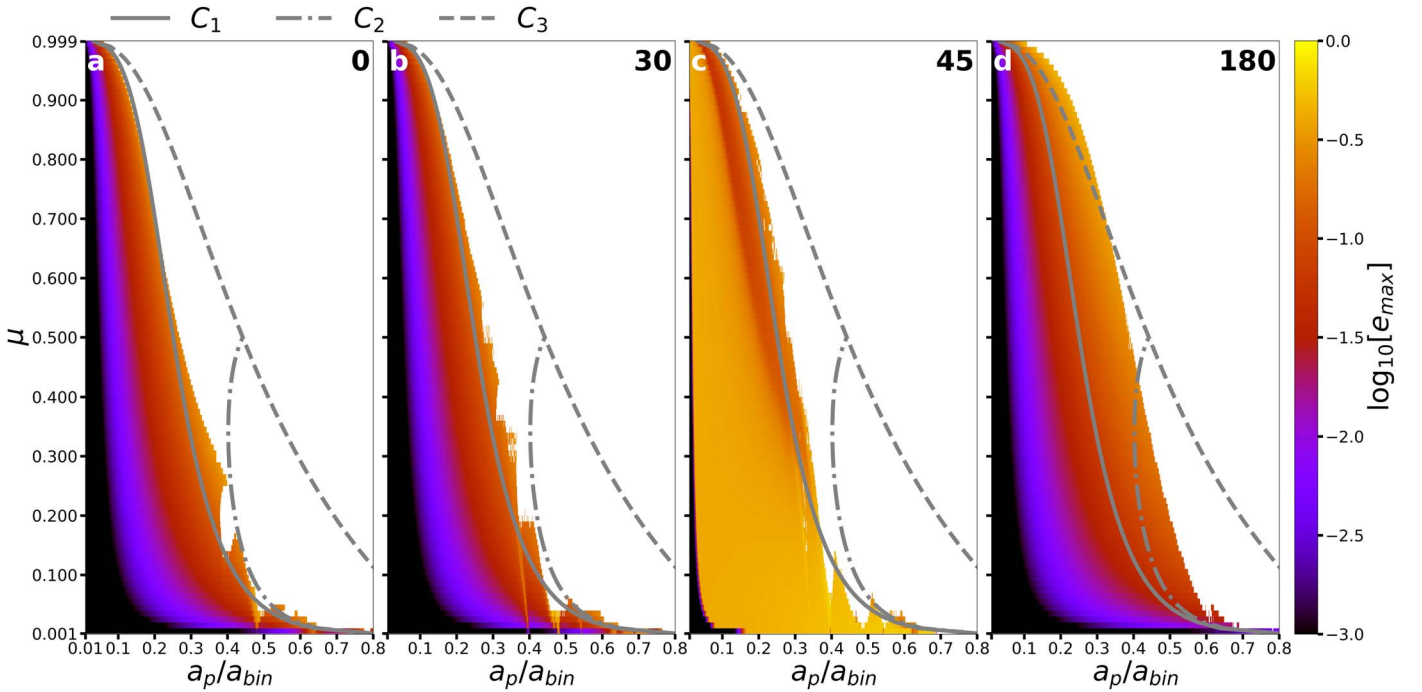


Figure 8. Similar to Figure 4, but the stable points are color-coded (on a logarithmic scale) using the maximum planetary eccentricity attained over all 91 trials of mean anomaly. Gray curves mark the opening of the zero velocity curve for each of the collinear Lagrange points.

has uncovered thousands of exoplanets (Coughlin et al. 2016) and eclipsing binary stars (Kirk et al. 2016). As a result, it becomes reasonable to identify how the stability limit changes with respect to the planetary eccentricity e_p . Statistical studies of the radial velocity planets before *Kepler* suggested that the mean planet eccentricity was approximately 0.3 (Shen & Turner 2008). Subsequent studies using both the radial velocity planets and those discovered by the *Kepler Space Telescope* showed that this is indeed correct for “single” planetary systems and that a lower mean eccentricity ($\langle e_p \rangle \approx 0.05$) is appropriate for systems with multiple planets (Xie et al. 2016; Van Eylen et al. 2019). Moreover, the presence of binary

companions does not affect this estimate (Van Eylen et al. 2019).

In the CRTBP, the maximum planet eccentricity is largely shaped by either a MMR or the Lidov–Kozai mechanism. Both of these pathways for eccentricity excitation depend on the semimajor axis ratio a_p/a_{bin} and less so on the mass ratio μ . Figure 8 illustrates the maximum planetary eccentricity e_{max} attained (color-coded on a logarithmic scale) for the cases where the planetary stability is achieved for all 91 trials of mean longitude (i.e., black cells in Figure 4). The gray curves in Figure 8 mark the limits set by the Jacobi Constants at the collinear Lagrange points. In Figure 8, panels (a), (b), and (d)

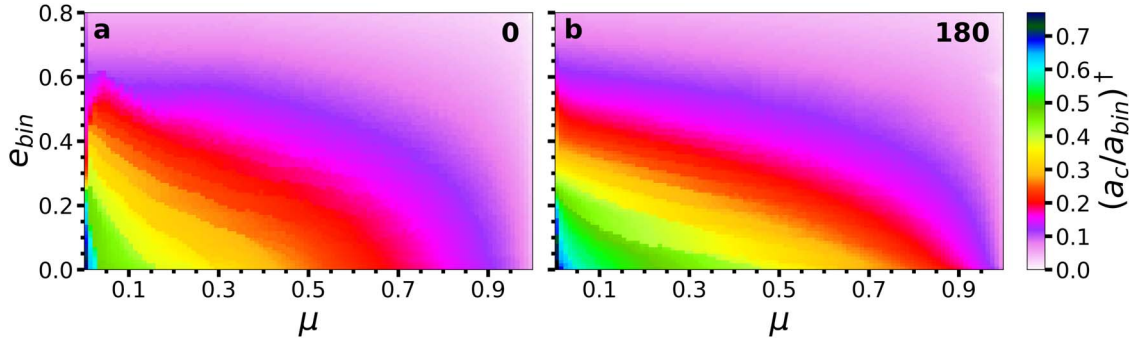


Figure 9. Similar to Figure 7, but limited to a coplanar planet in (a) prograde or (b) retrograde relative to the binary orbit. The color code represents the critical semimajor axis $(a_c/a_{\text{bin}})^\dagger$, where the maximum planetary eccentricity is less than 0.3.

show that the typical maximum planetary eccentricity is small ($e_{\text{max}} \lesssim 0.1$), where Figure 8(c) is large due to the Lidov–Kozai mechanism. A substantial e_{max} persists when $i_p = 45^\circ$ (Figure 8(c)) even for small semimajor axis ratios and mass ratios. The CRTBP is a special case, and nearly circular binaries are not likely to represent a large fraction of the general population of binary stars. Detailed studies from secular theory (Brouwer & Clemence 1961; Kaula 1962; Heppenheimer 1978; Murray & Dermott 1999; Andrade-Ines et al. 2016; Andrade-Ines & Eggl 2017) and N -body simulations (Quarles et al. 2018a) have illustrated that the secular forcing from the stellar component induces a forced component to the planet’s eccentricity that depends on the mass ratio μ , semimajor axis ratio a_p/a_{bin} , and the binary eccentricity e_{bin} . The planetary eccentricity varies about the forced eccentricity depending on the relative alignment ($\varpi_p - \varpi_{\text{bin}}$) with the binary orbit. Each cell in Figure 7(a) represents a series of 91 trials with respect to the mean longitude, and the a_c/a_{bin} value determined is one where all trial mean longitudes survive for the full integration for a given a_p/a_{bin} . We augment this stability criterion to include another condition that the maximum planetary eccentricity e_{max} does not exceed 0.3 (i.e., the mean planetary eccentricity from observations), and signify this altered stability criterion as $(a_c/a_{\text{bin}})^\dagger$.

The critical semimajor axis does not vary much when comparing Figure 7(a) to Figure 7(b), and the maximum planetary eccentricity will follow the same trend. The maximum planetary eccentricity can be determined analytically, for nearly circular binaries, when the Lidov–Kozai mechanism is active (Innanen et al. 1997) for $i_p = 45^\circ$. In most cases, the maximum eccentricity is much larger than 0.3. Therefore we only consider the coplanar configuration in either a prograde ($i_p = 0^\circ$) or retrograde ($i_p = 180^\circ$) direction relative to the binary orbit in Figure 9. Applying the extra condition on the planetary eccentricity typically decreases the critical semimajor axis by $\sim 10\%$ when comparing Figure 7(a) to Figure 9(a), where the decrease is much more substantial for the comparison between Figures 7(d) and 9(b). In Figure 9, the differences between panels (a) and (b) are less dramatic than those in Figure 7, but planets orbiting within binaries with low eccentricity still retain their stability advantage because the forced component of eccentricity is also low.

The inclusion of an additional constraint like maximum eccentricity on planetary stability in binaries decreases the critical semimajor axis ratio, where long-period planets would be most affected. However, observations of small planets have proved to come in multiples (Fabrycky et al. 2014; Winn & Fabrycky 2015), which suggests that planet multiplicity is a

better additional constraint on the potential stability of a planet within a binary (Quarles & Lissauer 2018), as the mean planet eccentricity of the observed exoplanets is lower (Xie et al. 2016; Van Eylen et al. 2019).

5. Binary Star Populations and TESS

5.1. Population Studies

The results in Figure 7 illustrates the variations of the critical semimajor axis with respect to the mass ratio μ and eccentricity e_{bin} , but observations of binary star populations, especially with Sunlike primaries, are not uniform with respect to these binary parameters (Raghavan et al. 2010; Moe & Di Stefano 2017). Therefore, a statistical study is needed to gain further insights from our results using Monte Carlo approaches. David et al. (2003) and Fatuzzo et al. (2006) performed a statistical study with the binary periastron distance as a stability criterion, and using the contemporary stability formula (Holman & Wiegert 1999) and a survey of binary stars (Duquennoy & Mayor 1991). We follow their approach, but use our our determination of the critical semimajor axis and more up-to-date results from binary star surveys (Raghavan et al. 2010; Moe & Di Stefano 2017). This is important for observations because, when planets are discovered orbiting a star with a distant stellar companion, e.g., K2-288b (Feinstein et al. 2019), the binary period and eccentricity are often unknown, but the planetary semimajor axis and/or the projected binary semimajor axis can be determined (see Table 5 for a list of known planet hosting binary stars). Moreover, observations of young binary stars can reveal the stability limit through dust and gas emission around either star (e.g., Alves et al. 2019), but this is also a projected distance.

Our approach is to determine a probability distribution function (PDF) for the stability of planets in binaries as a function of the critical semimajor axis ratio a_c/a_{bin} , where the sum of the binary masses is equal to a solar mass (i.e., $M_A + M_B = 1 M_\odot$). The binary period (and semimajor axis) follows a log-normal probability distribution ($p_{\log P} \propto e^{-(\log P - \zeta)^2 / 2\sigma^2}$), where $\zeta = 5.03$ and $\sigma = 2.28$ (Raghavan et al. 2010). This probability distribution in Raghavan et al. (2010) has a broad range ($-2 \leq \log P \leq 10$, in days), where we limit our analysis to a smaller range in binary period ($4 \leq \log P \leq 7$) that corresponds to a reasonable range in binary semimajor axis ($10 \text{ au} \leq a_{\text{bin}} \leq 1000 \text{ au}$).

Observers typically use the binary mass quotient q ($=M_B/M_A$, where $M_B \leq M_A$), which algebraically relates to the dynamical mass ratio μ ($=q/(1+q)$). From the mass quotient q , the range for μ is limited to 0.5 and our exploration

Table 5
Mass Ratio, Semimajor Axis, and Stability Limits for Known Planet-hosting Binaries with $5 \leq a_{\text{bin}} < 500$ au

System	M_A (M_\odot)	M_B (M_\odot)	μ	a_{bin} (au)	$a_c^{A,a}$ (a_{bin})	$a_c^{A,b}$ (a_{bin})	$a_c^{B,a}$ (a_{bin})	$a_c^{B,b}$ (a_{bin})
HD 109749	1.100	0.780	0.415	490	0.046	0.299	0.040	0.235
HD 133131	0.950	0.930	0.495	360	0.043	0.267	0.042	0.263
HD 106515	0.910	0.880	0.492	345	0.043	0.267	0.042	0.261
Kepler-108	1.300	0.960	0.425	327	0.045	0.295	0.040	0.238
WASP-77	1.002	0.710	0.415	306	0.046	0.299	0.040	0.235
KELT-2	1.317	0.780	0.372	295	0.047	0.321	0.037	0.222
HD 114729	0.930	0.253	0.214	282	0.053	0.379	0.031	0.169
Kepler-14	1.510	1.390	0.479	280	0.043	0.272	0.042	0.257
HD 27442	1.200	0.750	0.385	240	0.047	0.314	0.038	0.227
TrES-2	0.980	0.509	0.342	232	0.048	0.338	0.037	0.213
HD 212301	1.270	0.350	0.216	230	0.053	0.380	0.032	0.170
HD 16141	1.010	0.286	0.221	220	0.052	0.380	0.032	0.171
HD 189733	0.800	0.200	0.200	216	0.054	0.377	0.031	0.164
HD 217786	1.020	0.160	0.136	155	0.057	0.435	0.027	0.141
HD 142	1.200	0.590	0.330	138	0.048	0.346	0.036	0.209
HD 114762	0.840	0.138	0.141	132	0.057	0.432	0.028	0.143
HD 195019	1.060	0.700	0.398	131	0.046	0.307	0.040	0.230
WASP-2	0.890	0.480	0.350	106	0.047	0.334	0.037	0.215
HD 19994	1.340	0.350	0.207	100	0.054	0.378	0.031	0.167
HD 177830	1.450	0.230	0.137	97	0.057	0.434	0.027	0.142
Gliese 15	0.380	0.150	0.283	93	0.051	0.378	0.035	0.194
Kepler-296	0.500	0.330	0.398	80	0.046	0.307	0.040	0.230
GJ 3021	0.900	0.130	0.126	68	0.057	0.440	0.026	0.137
K2-288	0.520	0.330	0.388	54.8	0.047	0.312	0.038	0.227
HD 120136	1.400	0.400	0.222	45	0.052	0.380	0.032	0.172
WASP-11	0.820	0.340	0.293	42	0.050	0.369	0.035	0.197
K2-136	0.740	0.100	0.119	40	0.057	0.442	0.026	0.135
HD 164509	1.130	0.420	0.271	37	0.051	0.383	0.034	0.190
HD 41004	0.700	0.400	0.363	23	0.048	0.326	0.037	0.219
HD 196885	1.330	0.550	0.293	23	0.050	0.369	0.035	0.197
HD 4113	0.990	0.550	0.357	23	0.048	0.330	0.037	0.217
GJ 86	0.800	0.490	0.380	21	0.047	0.317	0.038	0.225
γ Cep	1.180	0.320	0.213	20	0.053	0.379	0.031	0.169
HD 8673	1.400	0.400	0.222	10	0.052	0.380	0.032	0.172
Kepler-420	0.990	0.700	0.414	5.3	0.046	0.300	0.039	0.235

Notes. Critical semimajor axis a_c calculated using interpolation of Figure 7(a), where planets orbit star A for μ and star B for $1 - \mu$. The stellar parameters are from an online catalog of planets in binaries maintained by Richard Schwarz (<https://www.univie.ac.at/adg/schwarz/multiple.html>).

^a $e_{\text{bin}} = 0.8$.

^b $e_{\text{bin}} = 0.0$.

of planets orbiting the secondary star ($\mu > 0.5$) is accomplished by subtracting the μ samples from unity (i.e., $1 - \mu$). We use a probability distribution ($p_q \propto q^\gamma$) for q derived by Moe & Di Stefano (2017) that is a broken power law, which has $\gamma_1 = 0.3 \pm 0.4$ for $0.1 \leq q \leq 0.3$ and $\gamma_2 = -0.5 \pm 0.3$ for $0.3 \leq q \leq 1$. An excess twin fraction $F_{\text{twin}} = 0.1 \pm 0.3$ is added to the PDF for $q \geq 0.95$; see Figure 2 of Moe & Di Stefano (2017). A probability distribution ($p_e \propto e_{\text{bin}}^\eta$) for the binary eccentricity follows a single power law, which has $\eta = 0.4 \pm 0.3$ (Moe & Di Stefano 2017). We note that the exponents used in these power laws are dependent on the range of sampled binary period $\log P$ (Moe & Di Stefano 2017) and adjustments to the exponents are necessary if one expands our analysis to a broader range in binary period.

Using these probability distributions, we employ Monte Carlo integration to determine the fraction of observed binaries with a critical semimajor axis larger than a given a_c/a_{bin} using the data in panels (a), (c), and (d) of Figure 7. We do not use Figure 7(b) because of its strong similarity to Figure 7(a). Figure 7(a) illustrates that all binaries within the domain will

have a critical semimajor axis larger than 0.001 and very few binaries will have a $a_c/a_{\text{bin}} > 0.5$ where this is independent of the weighting given by the probability distributions we choose. As a result, we integrate $a_c/a_{\text{bin}} = 0.001\text{--}0.01$ using 0.001 sized bins, and $a_c/a_{\text{bin}} = 0.01\text{--}1.0$ using 0.01 sized bins. Figure 10 shows the PDF (Figure 10(a)–(c)) and cumulative distribution function (CDF; Figure 10(d)–(f)) resulting from the Monte Carlo integration considering planetary inclinations of 0° , 45° , and 180° . For planets orbiting either the primary (star A; black) or the secondary (star B; gray) star, there are many binaries with $a_c/a_{\text{bin}} > 0.05$, and hence both curves in Figure 10(a)–(c) have the highest probability within this range. Planets that orbit the secondary constitute a larger fraction of binaries with a small critical semimajor axis, and thus the probability is slightly larger. This trend reverses for $a_c/a_{\text{bin}} \gtrsim 0.12$, as the stability limit for the primary extends to larger distances compared to the secondary. Sufficiently inclined planets (e.g., $i_p = 45^\circ$) have their stability limits truncated due to the large growth of eccentricity from the Lidov–Kozai mechanism, and stable orbits are possible for

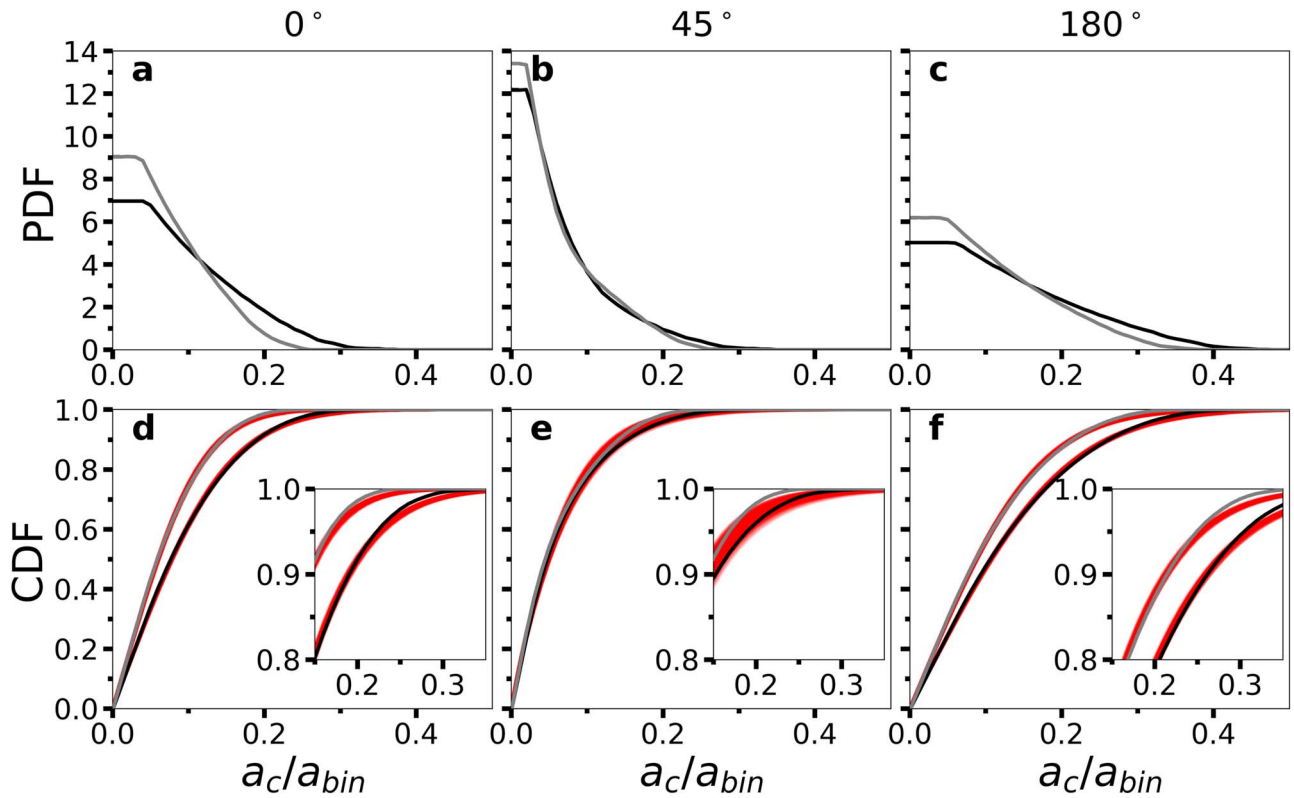


Figure 10. PDF for the critical semimajor axis ratio a_c/a_{bin} of a planet orbiting either star A (black) or star B (gray). Top panels show the PDF relative to whether the planet orbit is (a) prograde ($i_p = 0^\circ$), (b) undergoing Lidov–Kozai cycles ($i_p = 45^\circ$), or is (c) retrograde ($i_p = 180^\circ$) with respect to the binary. Panels (d)–(f) show the cumulative distribution function (CDF) for panels (a)–(c), respectively, and the zoomed insets show the top quintile of the CDF. Samples from a numerical fit of the CDF using a modified exponential distribution (see main text) are marked in red, where the coefficients for the fit are given in Table 6.

predominantly low critical semimajor axis ratios. Retrograde orbits extend to larger critical semimajor axis ratios (Henon 1970; Quarles & Lissauer 2016), and the PDF is flatter.

The uncertainty in the binary semimajor axis a_{bin} from observations can be quite large, where discoveries from direct imaging may only have an estimate for the projected semimajor axis. From such situations, a CDF is more useful, where the probability can be calculated from a difference of values on the CDF and a single value describes the fraction of binaries with a stability limit less than a given a_c/a_{bin} . For example, Figure 10(d) shows that half of all binaries within our domain will have a critical semimajor axis for coplanar planets that is less than 0.06 (star B) or 0.078 (star A). The slope in the CDF for the Lidov–Kozai regime (Figure 10(e)) is steeper, which shifts the median to smaller a_c/a_{bin} . Moreover, the slope is nearly identical between whichever star the planet is orbiting (star A or B). The shallower slope for retrograde planets (Figure 10(f)) has a median critical semimajor axis closer to 0.1 and extends to larger values of a_c/a_{bin} .

The black and gray curves in Figure 10(d)–(f) are fit well by a modified exponential distribution:

$$F(\xi) = 1 - e^{-c_1\xi^2 - c_2\xi}, \quad (1)$$

where $\xi = a_c/a_{\text{bin}}$. The red curves in Figure 10(d)–(f) mark sample curves within the 1σ of the best-fit values for $F(\xi)$, where the largest differences occur in the top quintile as marked by the respective inset panels. David et al. (2003) used a similar function, except their formulation depends on the binary periastron distance. Table 6 provides values for the coefficients (c_1 and c_2), along with their uncertainties using

Table 6
Cumulative Distribution Function Coefficients for the Critical Semimajor Axis

	i_p	$c_1 \pm \sigma_1$	$c_2 \pm \sigma_2$	50%	99.7%
Star A	0°	28.96 ± 0.75	6.65 ± 0.09	0.078	0.348
Star B	0°	54.50 ± 1.62	8.31 ± 0.14	0.060	0.259
Star A	45°	15.11 ± 2.30	13.28 ± 0.23	0.049	0.321
Star B	45°	20.69 ± 3.28	13.82 ± 0.30	0.047	0.292
Star A	180°	15.41 ± 0.37	4.82 ± 0.06	0.107	0.477
Star B	180°	22.97 ± 0.62	5.88 ± 0.08	0.088	0.391

Note. The coefficients (c_1 and c_2) and uncertainties (σ_1 and σ_2) using a fitting formula for the CDF, $F(\xi) = 1 - e^{-c_1\xi^2 - c_2\xi}$ where $\xi = a_c/a_{\text{bin}}$.

the Levenberg–Marquardt algorithm in the curve fit function within the `scipy` module. In addition to the coefficients, we provide the the critical semimajor axis values at 50% and 99.7% quantiles.

5.2. Circumstellar Planets Observed with TESS

NASA’s *TESS* will observe nearly 85% of the sky over the course of its primary two-year mission. The spacecraft has four cameras that provide a $24^\circ \times 96^\circ$ field of view, and a photometric precision between ~ 100 ppm for apparent magnitude $I_C \sim 4$, and $\sim 10^5$ ppm for $I_C \sim 18$ (Ricker et al. 2015). It is expected that *TESS* will discover thousands of transiting exoplanets around bright, nearby stars (Sullivan et al. 2015; Bouma et al. 2017; Barclay et al. 2018), including hundreds of planets smaller than $2R_\oplus$. A significant number of

stars (some of which will have transiting planets) observed by *TESS* will be in multiple systems, i.e., from $\sim 20\%$ for $M_{\text{prim}} < 0.1 M_{\odot}$ to $\sim 75\%$ for $M_{\text{prim}} > 1.4 M_{\odot}$, and spanning semimajor axes from a few to hundreds of au (Sullivan et al. 2015). In combination with data from *Gaia*, by virtue of being bright targets (and thus favorable to follow-up observations) those of the multiple star systems hosting S-type planet candidates will be amenable to measurements of the mass ratio. The results we present here will be directly applicable to the stability of these systems.

Recently, Winters et al. (2019) uncovered a transiting planet in a triple star system, LTT 1445ABC, where star A ($M_A = 0.257 M_{\odot}$) orbits a nearly equal-mass stellar binary ($M_B = 0.215 M_{\odot}$ and $M_C = 0.161 M_{\odot}$) and the separation from star A to the BC barycenter is ~ 34 au. The nearly Earth-sized exoplanet LTT 1445Ab ($R_p \approx 1.38 R_{\oplus}$) orbits very quickly (5.358 days, or $a_p = 0.038$ au) around LTT 1445A, which is well within the stability limit, assuming that the orbit of LTT 1445A is nearly circular around the barycenter of LTT 1445BC. However, the A–BC orbit is likely eccentric, considering observations over the last few decades that indicate significant astrometric variation (Mason et al. 2001; Dieterich et al. 2012; Winters et al. 2019, and references therein), and a noncircular orbit may affect the stability of the observed exoplanet. Using the combined mass for LTT 1445BC ($M_{BC} = 0.376 M_{\odot}$), the dynamical mass ratio of the A–BC pair is $\mu = 0.594$, given that the planet is orbiting the less massive component of the pair. The semimajor axis a_p is quite small (0.038 au), where the planetary orbital stability may be compromised for a large eccentricity e_{bin} of the A–BC orbit.

If we consider planets within the A–BC plane, then the stability limit varies between 1.38 and 8.15 au depending on the value of e_{bin} , the eccentricity of star A around the BC barycenter. Even for a high value for e_{bin} , the stability limit is still ~ 36 times farther from the host star than the observed planetary semimajor axis. Therefore, we are confident that LTT 1445Ab is on a stable orbit, as the planet is very far from the stability limit under reasonably extreme assumptions on the shape of the LTT 1445 A–BC stellar orbit. If *TESS* observes the system during the extended mission and detects potential transits of additional planets on longer orbits, reducing the BC binary to its barycenter may need to be revised and the eccentricity of star A around the BC barycenter properly evaluated. We do not investigate nonplanar conditions ($i_p = 45^\circ$) where the stability limit can be further reduced, because the astrometric measurements show that the LTT 1445ABC system is nearly planar and the planet is transiting—which implies that the planetary orbit is likely nearly aligned with the LTT 1445ABC orbital plane.

6. Summary and Discussion

The orbital stability of circumstellar planets within stellar binaries depends on many factors, where we focus on the binary mass ratio μ , eccentricity e_{bin} , semimajor axis ratio a_p/a_{bin} , and the mutual inclination of the planet i_p . Holman & Wiegert (1999) developed a fitting formula that incorporates the first three of these parameters and has a limited accuracy (up to 11%). We update the coefficients of the fitting formula using a larger array of N -body integrations (~ 700 million simulations), where the larger data set substantially narrows the uncertainties and calculates fitting coefficients that account for the planetary inclination i_p . We provide additional formulations

for stability: (1) using the Jacobi constant when e_{bin} is small or (2) a constraint on the maximum planetary eccentricity. Using the known population of Sunlike stellar binaries, we find that the stability limit is typically less than $\lesssim 8\%$ of the binary semimajor axis a_{bin} , where this fraction can be substantially reduced for an inclined planet that is undergoing Lidov–Kozai cycles, or expanded if the planet orbits in retrograde.

Eberle et al. (2008) developed a stability criterion based upon the value of the Jacobi constant at the collinear Lagrange points within the CRTBP. We extend this criterion to include orbits around the less massive secondary star, with a significantly inclined planetary orbit. However, this stability criterion has some limitations, where an asymmetry in the Coriolis acceleration (Innanen 1980; Hamilton & Burns 1991; Grishin et al. 2017) and a reduction in the duration of action (Henon 1970) can promote greater stability. The integration of the Jacobi integral (typically by quadrature) introduces a squared velocity term that is invariant for the direction of the smaller body’s motion (i.e., planet) and forms a symmetry with respect to the planetary inclination. Table 2 provides the critical semimajor axis ratios using the binary mass ratio and Jacobi constants (C_1 and C_3) for prograde orbits and a fit to the stability boundary from our numerical simulations (Figure 4) for coplanar retrograde orbits (C_1^{retro}). We note that, for a special case in our results ($\mu = 0.999$), the ratio of the retrograde critical semimajor axis ratio to the respective prograde ratio agrees well with the analytical expectation (i.e., $C_1^{\text{retro}}/C_1 \approx 3^{1/3}$) derived for hierarchical three-body systems (Hamilton & Burns 1991; Grishin et al. 2017). Although highly inclined orbits experience a greater eccentricity excitation, they also feel a smaller contribution from the Coriolis force—and can therefore achieve capture into MMRs with the binary (Morais & Giuppone 2012; Morais & Namouni 2013).

We provide updated coefficients ($c_1 - c_6$) to the stability formulas by Holman & Wiegert (1999), where the uncertainties of these coefficients are typically reduced by a factor of three. Moreover, we calculate coefficients using numerical simulations for a range of planetary inclination ($i_p = 0^\circ, 30^\circ, 45^\circ$, and 180°). For nearly coplanar planets in prograde, the coefficients have similar mean values. The coefficients for prograde planets undergoing Lidov–Kozai oscillations ($i_p = 45^\circ$) are more strongly dependent on the binary eccentricity. The coefficients fitting our numerical results for coplanar, retrograde planets depend linearly on the binary eccentricity, in contrast to the prograde results. Our coefficients are more accurate—but, similar to those of Holman & Wiegert (1999), they suffer from errors due to averaging. Therefore, we provide interpolation maps, where the data behind these maps are available to the community through [GitHub](#) and [Zenodo](#), which are similar to our previous repositories (Quarles et al. 2018b). In the [GitHub](#) repository, there is an example script in Python that demonstrates how to use the interpolation schemes in `scipy` to estimate the stability limit between grid values. Using our interpolation scheme, the stability limit for a prograde, coplanar planet orbiting α Cen A or α Cen B is 2.78 au or 2.60 au, respectively, and consistent with a previous detailed billion year study of the system (Quarles et al. 2018a). However a retrograde, coplanar planet orbiting α Cen A or α Cen B has a larger stability limit of 3.84 au or 3.61 au, respectively, and can be extended farther when the eccentricity vectors of the

planetary and binary orbits begin in a relative alignment that minimizes the free eccentricity (Quarles et al. 2018a).

Population studies of Sunlike binary stars show that the mass quotient q , binary eccentricity e_{bin} , and binary period P_{bin} can be statistically fit using either power laws or a log normal distribution (Raghavan et al. 2010; Moe & Di Stefano 2017). We use these statistical fits to estimate the probability of a planet (via a PDF or CDF) orbiting star A rather than star B, given the critical semimajor axis ratio a_c/a_{bin} . The PDF (or CDF) is modified depending on the assumed mutual inclination of the planet: a coplanar prograde planet has the most probability when $a_c/a_{\text{bin}} \lesssim 0.08$, an inclined ($i_p = 45^\circ$) prograde planet's high-probability regime decreases by half ($a_c/a_{\text{bin}} \lesssim 0.04$), and a coplanar retrograde planet has a broader high-probability region extending to $a_c/a_{\text{bin}} \lesssim 0.10$. Table 6 provides coefficients fitted to each CDF using a modified exponential distribution. Using a_c/a_{bin} is important for future studies because direct imaging observations often rely on projected distances, and new disk observations of young binary systems can match this ratio to the disk truncation distance (e.g., Alves et al. 2019).

Observations are ongoing to find and characterize circumstellar planets in binary star systems, where the *TESS* mission as well as *Gaia* (Gaia Collaboration et al. 2018) will be instrumental for future discoveries. In particular, Winters et al. (2019) identified a planet within a hierarchical triple star system, LTT 1445ABC, using data from *TESS*. Due to the long orbital binary orbital periods necessary for stability, *Gaia* will uncover the multiplicity of stellar systems (e.g., Evans 2018), while *TESS* may identify whether any planets are transiting at the present epoch. Additional efforts will soon be underway using the *James Webb Space Telescope (JWST)*, where direct imaging help identify the extent of the protoplanetary disks within young stellar binaries or whole systems of planets in older systems. Beichman et al. (2020) outlined particular considerations needed to use *JWST* for this purpose in observing α Cen A, and some a priori knowledge for the stability of planets is beneficial for such observations.

Some of the computing for this project was performed at the OU Supercomputing Center for Education & Research (OSCAR) at the University of Oklahoma (OU). This research was supported in part through research cyberinfrastructure resources and services provided by the Partnership for an Advanced Computing Environment (PACE) at the Georgia Institute of Technology. N.H. acknowledges support from NASA XRP program through grant 80NSSC18K0519.

Software: scipy (Virtanen et al. 2019); mercury6 (Chambers et al. 2002); REBOUND (Rein & Liu 2012; Rein & Spiegel 2015).

ORCID iDs

Billy Quarles  <https://orcid.org/0000-0002-9644-8330>
 Gongjie Li  <https://orcid.org/0000-0001-8308-0808>
 Veselin Kostov  <https://orcid.org/0000-0001-9786-1031>
 Nader Haghighipour  <https://orcid.org/0000-0002-5234-6375>

References

Alves, F. O., Caselli, P., Girart, J. M., et al. 2019, *Sci*, 366, 90
 Andrade-Ines, E., Beaugé, C., Michtchenko, T., & Robutel, P. 2016, *CeMDA*, 124, 405

Andrade-Ines, E., & Eggl, S. 2017, *AJ*, 153, 148
 Andrade-Ines, E., & Michtchenko, T. A. 2014, *MNRAS*, 444, 2167
 Barclay, T., Pepper, J., & Quintana, E. V. 2018, *ApJS*, 239, 2
 Beichman, C., Ygouf, M., Llop Sayson, J., et al. 2020, *PASP*, 132, 015002
 Benest, D. 1988a, *CeMec*, 43, 47
 Benest, D. 1988b, *A&A*, 206, 143
 Benest, D. 1993, *CeMDA*, 56, 45
 Benettin, G., Galgani, L., Giorgilli, A., & Strelcyn, J. M. 1980, *Mecc*, 15, 9
 Bouma, L. G., Winn, J. N., Kosiarek, J., & McCullough, P. R. 2017, arXiv:1705.08891
 Brouwer, D., & Clemence, G. M. 1961, *Methods of Celestial Mechanics* (New York: Academic)
 Butler, R. P., Marcy, G. W., Williams, E., Hauser, H., & Shirts, P. 1997, *ApJL*, 474, L115
 Campbell, B., Walker, G. A. H., & Yang, S. 1988, *ApJ*, 331, 902
 Chambers, J. E., Quintana, E. V., Duncan, M. J., & Lissauer, J. J. 2002, *AJ*, 123, 2884
 Ciardi, D. R., Crossfield, I. J. M., Feinstein, A. D., et al. 2018, *AJ*, 155, 10
 Cincotta, P., & Simó, C. 1999, *CeMDA*, 73, 195
 Cincotta, P. M., Giordano, C. M., & Simó, C. 2003, *PhyD*, 182, 151
 Cincotta, P. M., & Simó, C. 2000, *A&AS*, 147, 205
 Cochran, W. D., Hatzes, A. P., Butler, R. P., & Marcy, G. W. 1997, *ApJ*, 483, 457
 Coughlin, J. L., Mullally, F., Thompson, S. E., et al. 2016, *ApJS*, 224, 12
 Cuntz, M., Eberle, J., & Musielak, Z. E. 2007, *ApJL*, 669, L105
 David, E.-M., Quintana, E. V., Fatuzzo, M., & Adams, F. C. 2003, *PASP*, 115, 825
 Dieterich, S. B., Henry, T. J., Golimowski, D. A., Krist, J. E., & Tanner, A. M. 2012, *AJ*, 144, 64
 Doolin, S., & Blundell, K. M. 2011, *MNRAS*, 418, 2656
 Dumusque, X., Pepe, F., Lovis, C., et al. 2012, *Natur*, 491, 207
 Duquennoy, A., & Mayor, M. 1991, *A&A*, 500, 337
 Eberle, J., Cuntz, M., & Musielak, Z. E. 2008, *A&A*, 489, 1329
 Evans, D. F. 2018, *RNAAS*, 2, 20
 Fabrycky, D. C., Lissauer, J. J., Ragozzine, D., et al. 2014, *ApJ*, 790, 146
 Fatuzzo, M., Adams, F. C., Gauvin, R., & Proszkow, E. M. 2006, *PASP*, 118, 1510
 Feinstein, A. D., Schlieder, J. E., Livingston, J. H., et al. 2019, *AJ*, 157, 40
 Froeschlé, C., Lega, E., & Gonczi, R. 1997, *CeMDA*, 67, 41
 Gaia Collaboration, Brown, A. G. A., Vallenari, A., et al. 2018, *A&A*, 616, A1
 Giuppone, C. A., & Correia, A. C. M. 2017, *A&A*, 605, A124
 Giuppone, C. A., Morais, M. H. M., Boué, G., & Correia, A. C. M. 2012, *A&A*, 541, A151
 Gonczi, R., & Froeschle, C. 1981, *CeMec*, 25, 271
 Goździewski, K., Bois, E., Maciejewski, A. J., & Kiseleva-Eggleton, L. 2001, *A&A*, 378, 569
 Grishin, E., Perets, H. B., Zenati, Y., & Michaely, E. 2017, *MNRAS*, 466, 276
 Haghighipour, N., & Raymond, S. N. 2007, *ApJ*, 666, 436
 Hamilton, D. P., & Burns, J. A. 1991, *Icar*, 92, 118
 Hatzes, A. P. 2013, *ApJ*, 770, 133
 Hatzes, A. P., Cochran, W. D., Endl, M., et al. 2003, *ApJ*, 599, 1383
 Henon, M. 1970, *A&A*, 9, 24
 Heppenheimer, T. A. 1978, *A&A*, 65, 421
 Holman, M. J., & Wiegert, P. A. 1999, *AJ*, 117, 621
 Innanen, K. A. 1980, *AJ*, 85, 81
 Innanen, K. A., Zheng, J. Q., Mikkola, S., & Valtonen, M. J. 1997, *AJ*, 113, 1915
 Kaula, W. M. 1962, *AJ*, 67, 300
 Kenyon, S. J., & Bromley, B. C. 2019a, *AJ*, 157, 79
 Kenyon, S. J., & Bromley, B. C. 2019b, *AJ*, 158, 69
 Kirk, B., Conroy, K., Prša, A., et al. 2016, *AJ*, 151, 68
 Kozai, Y. 1962, *AJ*, 67, 591
 Kratter, K. M., & Shannon, A. 2014, *MNRAS*, 437, 3727
 Kraus, A. L., Ireland, M. J., Huber, D., Mann, A. W., & Dupuy, T. J. 2016, *AJ*, 152, 8
 Lam, C., & Kipping, D. 2018, *MNRAS*, 476, 5692
 Lecar, M., Franklin, F., & Murison, M. 1992, *AJ*, 104, 1230
 Lidov, M. L. 1962, *P&SS*, 9, 719
 Marcy, G. W., & Butler, R. P. 1995, *BAAS*, 27, 1379
 Mardling, R. A. 2008, *The Cambridge N-Body Lectures, Lecture Notes in Physics*, Vol. 760 (Berlin: Springer), 59
 Martin, D. V. 2017, *MNRAS*, 467, 1694
 Marzari, F., Scholl, H., Thébault, P., & Baruteau, C. 2009, *A&A*, 508, 1493
 Mason, B. D., Wycoff, G. L., Hartkopf, W. I., Douglass, G. G., & Worley, C. E. 2001, *AJ*, 122, 3466
 Mayor, M., & Queloz, D. 1995, *Natur*, 378, 355

- Moe, M., & Di Stefano, R. 2017, *ApJS*, **230**, 15
- Morais, M. H. M., & Giuppone, C. A. 2012, *MNRAS*, **424**, 52
- Morais, M. H. M., & Namouni, F. 2013, *CeMDA*, **117**, 405
- Mudryk, L. R., & Wu, Y. 2006, *ApJ*, **639**, 423
- Murray, C. D., & Dermott, S. F. 1999, *Solar System Dynamics* (Cambridge: Cambridge Univ. Press)
- Musielak, Z. E., & Quarles, B. 2014, *RPPh*, **77**, 065901
- Ngo, H., Knutson, H. A., Bryan, M. L., et al. 2017, *AJ*, **153**, 242
- Pilat-Lohinger, E., & Dvorak, R. 2002, *CeMDA*, **82**, 143
- Pilat-Lohinger, E., Funk, B., & Dvorak, R. 2003, *A&A*, **400**, 1085
- Press, W. H., Teukolsky, S. A., Vetterling, W. T., & Flannery, B. P. 1993, *Numerical Recipes in FORTRAN; The Art of Scientific Computing* (2nd ed.; New York: Cambridge Univ. Press)
- Quarles, B., Eberle, J., Musielak, Z. E., & Cuntz, M. 2011, *A&A*, **533**, A2
- Quarles, B., & Lissauer, J. J. 2016, *AJ*, **151**, 111
- Quarles, B., & Lissauer, J. J. 2018, *AJ*, **155**, 130
- Quarles, B., Lissauer, J. J., & Kaib, N. 2018a, *AJ*, **155**, 64
- Quarles, B., Satyal, S., Kostov, V., Kaib, N., & Haghighipour, N. 2018b, *ApJ*, **856**, 150
- Quintana, E. V., Lissauer, J. J., Chambers, J. E., & Duncan, M. J. 2002, *ApJ*, **576**, 982
- Rabl, G., & Dvorak, R. 1988, *A&A*, **191**, 385
- Rafikov, R. R. 2013, *ApJL*, **765**, L8
- Rafikov, R. R., & Silsbee, K. 2015, *ApJ*, **798**, 70
- Raghavan, D., McAlister, H. A., Henry, T. J., et al. 2010, *ApJS*, **190**, 1
- Rajpaul, V., Aigrain, S., & Roberts, S. 2016, *MNRAS*, **456**, L6
- Rein, H., & Liu, S.-F. 2012, *A&A*, **537**, A128
- Rein, H., & Spiegel, D. S. 2015, *MNRAS*, **446**, 1424
- Ricker, G. R., Winn, J. N., Vanderspek, R., et al. 2015, *JATIS*, **1**, 014003
- Satyal, S., Quarles, B., & Hinse, T. C. 2013, *MNRAS*, **433**, 2215
- Shen, Y., & Turner, E. L. 2008, *ApJ*, **685**, 553
- Smith, R. H., & Szebehely, V. 1993, *CeMDA*, **56**, 409
- Sullivan, P. W., Winn, J. N., Berta-Thompson, Z. K., et al. 2015, *ApJ*, **809**, 77
- Szebehely, V. 1980, *CeMec*, **22**, 7
- Thébault, P., Marzari, F., & Scholl, H. 2008, *MNRAS*, **388**, 1528
- Thébault, P., Marzari, F., & Scholl, H. 2009, *MNRAS*, **393**, L21
- Van Eylen, V., Albrecht, S., Huang, X., et al. 2019, *AJ*, **157**, 61
- Virtanen, P., Gommers, R., Oliphant, T. E., et al. 2019, arXiv:1907.10121
- Walker, G. A. H., Bohlender, D. A., Walker, A. R., et al. 1992, *ApJL*, **396**, L91
- Wiegert, P. A., & Holman, M. J. 1997, *AJ*, **113**, 1445
- Winn, J. N., & Fabrycky, D. C. 2015, *ARA&A*, **53**, 409
- Winters, J. G., Medina, A. A., Irwin, J. M., et al. 2019, *AJ*, **158**, 152
- Wisdom, J., & Holman, M. 1991, *AJ*, **102**, 1528
- Wisdom, J., & Holman, M. 1992, *AJ*, **104**, 2022
- Xie, J.-W., Dong, S., Zhu, Z., et al. 2016, *PNAS*, **113**, 11431
- Xie, J.-W., Zhou, J.-L., & Ge, J. 2010, *ApJ*, **708**, 1566
- Zhao, L., Fischer, D. A., Brewer, J., Giguere, M., & Rojas-Ayala, B. 2018, *AJ*, **155**, 24
- Zsom, A., Sándor, Z., & Dullemond, C. P. 2011, *A&A*, **527**, A10